~~Environmental~~ Unusual atmospheric and sea ice conditions in the North Atlantic sector of the Arctic during the ~~HALO–(AC)^3~~ HALO-($\mathcal{AC}$)^3 campaign

Andreas Walbröl[1], Janosch Michaelis[2,3], Sebastian Becker[4], Henning Dorff[5], Kerstin Ebell[1], Irina Gorodetskaya[6,7], Bernd Heinold[8], Benjamin Kirbus[4], Melanie Lauer[1], Nina Maherndl[4], Marion Maturilli[9], Johanna Mayer[10], Hanno Müller[4], Roel A. J. Neggers[1], Fiona M. Paulus[1], Johannes Röttenbacher[4], Janna E. Rückert[11], Imke Schirmacher[1], Nils Slättberg[9], André Ehrlich[4], Manfred Wendisch[4], and Susanne Crewell[1]

[1]Institute for Geophysics and Meteorology, University of Cologne, Cologne, Germany
[2]Alfred Wegener Institute, Helmholtz Center for Polar and Marine Research, Bremerhaven, Germany
[3]Maritime Klimatologie, Maritim-klimatologische Analysen und Produkte, Deutscher Wetterdienst (DWD), Hamburg, Germany
[4]Leipzig Institute for Meteorology, Leipzig University, Leipzig, Germany
[5]Meteorological Institute of Hamburg, University of Hamburg, Hamburg, Germany
[6]Centre for Environmental and Marine Studies, University of Aveiro, Aveiro, Portugal
[7]Interdisciplinary Centre of Marine and Environmental Research (CIIMAR), University of Porto, Matosinhos, Portugal
[8]Leibniz-Institut für Troposphärenforschung (TROPOS), Leipzig, Germany
[9]Alfred Wegener Institute, Helmholtz Center for Polar and Marine Research, Potsdam, Germany
[10]German Aerospace Centre (Deutsches Zentrum für Luft- und Raumfahrt (DLR)), Oberpfaffenhofen, Germany
[11]Institute of Environmental Physics, University of Bremen, Bremen, Germany

Correspondence: Andreas Walbröl (a.walbroel@uni-koeln.de)

Abstract.

~~Centered around the~~ How air masses transform during meridional transport into and out of the Arctic is not well represented by numerical models. The airborne field campaign HALO-($\mathcal{AC}$)^3 applied the High Altitude and Long Range (HALO) research aircraft ~~and the~~ within the framework of the collaborative research project on Arctic ~~Amplification (AC)^3, the airborne field campaign HALO–(AC)^3~~ amplification ($\mathcal{AC}$)^3 to address this question by providing a comprehensive observational basis. The campaign took place from 07 March to 12 April ~~2022. Its major goal was to observe the transformation of air masses during their meridional transport~~ 2022 in the North Atlantic sector of the Arctic~~. We evaluate~~, a main gateway of atmospheric transport into and out of the the Arctic. Here, we investigate to which degree the meteorological and sea ice conditions during the campaign ~~based on the~~ align with the long-term climatology (1979–2022). For this purpose, we use the European Centre for ~~Medium-Range~~ Medium-Range Weather Forecasts (ECMWF) ~~Reanalysis~~ reanalysis v5 (ERA5), satellite data, and ~~atmospheric soundings with respect to climatology. HALO–(AC)^3~~ measurements at Ny-Ålesund, including atmospheric soundings. The observations and reanalysis data revealed two distinct periods with different weather conditions during HALO-($\mathcal{AC}$)^3: The campaign started with a warm period (11–20 March 2022) where strong southerly winds prevailed that caused poleward transport of warm and moist air masses, so-called moist and warm air intrusions (MWAIs). Two MWAIs

were detected events were identified as Atmospheric Rivers (ARs). Compared to the ERA5 climatology (1979–2022), record breaking vertically integrated poleward heat and moisture fluxes averaged over the Fram Strait latitudes were found, which are narrow bands of strong moisture transport. These warm and moist air masses caused the highest rainfall rates over the 2 m temperatures (5.5 °C) and daily precipitation rates (42 mm day^{-1}) at Ny-Ålesund for March since the beginning of the record (1993). Over the sea ice northwest of Svalbard since the beginning of the , ERA5 climatology. During the subsequent cold period, starting after the indicated record-breaking rainfall. After the passage of a strong cyclone on 21 March , northerly winds advected colder 2022, a cold period followed. Northerly winds advected cold air into the Fram Strait . Marine causing marine cold air outbreaks (MCAOs) prevailed until 08 April, interrupted by short periods of aged subpolar warm air. until the end of the campaign. This second phase included one of the longest MCAO events found in the ERA5 record (19 days). On average, the entire campaign period was warmer than the climatological mean due to the strong influence of the ARs. In the Fram Strait, the sea ice concentration (SIC) was well within the climatological variability , staying within the 10–90th percentiles over the entire campaign duration. However, during the warm period, an atypically a large polynya opened north of Svalbard . For potential future studies, we describe the environmental conditions of the most significant weather events (ARs, MCAOs, Polar Low, and Arctic cirrus) during HALO–(AC)^3 in detail. Comparing atmospheric conditions over the Fram Strait with Ny–Ålesund (Svalbard), temporal shifts up to one day have been identified. The temporal shift and orographic effects must be taken into account when combining airborne HALO–(AC)^3 measurements with ground based observations at Ny–Ålesund. northeast of Svalbard untypical for this season. Compared to previous airborne field campaigns focusing on the evolution of (mixed–phasemixed-phase) clouds, a larger variety of MCAO conditions were observed during HALO–(AC)^3. Our study may serve as basis for future analyses of the data collected during the campaignHALO-($\mathcal{AC}$)^3. In summary, air mass transport into and out of the Arctic were both more pronounced than usual, providing exciting prospects to study air mass transformation using HALO-($\mathcal{AC}$)^3.

1 Introduction

The Currently, the Arctic experiences a drastic temperature increasealmost , which is up to 4 times stronger compared to the rest of the globe (Rantanen et al., 2022). This enhanced warming Arctic warming is one of the most obvious signs of Arctic amplification, which is known as Arctic Amplification and is caused by several numerous feedback mechanisms (Serreze et al., 2009; Screen and Simmonds, 2010; Serreze and Barry, 2011). While the contribution contributions of some feedback mechanisms to Arctic Amplification amplification can be regarded as scientific consensus (e.g., sea ice–albedo feedback, Serreze et al., 2009), others are not yet sufficiently explored and their contribution is uncertain (e.g., influence of clouds, lapse rate feedback, linkage . As the Arctic warms faster than the mid–latitudes, the meridional temperature gradient decreases in most heights of the troposphere, likely resulting in a weaker jet stream and possibly enhancing the tendency to meander (Francis and Vavrus, 2015). A more meandering jet would result in an increasing number of poleward moist (e.g., influence of clouds, lapse-rate feedback, Wendisch et . Especially the role of linkages between Arctic and mid-latitudes is still under debate. Moist and warm air intrusions (MWAIs) and southward cold air outbreaks (CAOs). However, the tropical upper troposphere warms while the Arctic lower stratosphere cools, enhancing meridional temperature gradients at higher altitudes (Lee et al., 2019; Stendel et al., 2021). The frequency of meridional transport through the North Atlantic has increased during the last decades while it stayed constant or even decreased in other regions (Mewes and Jacobi, 2019). You et al. (2022) found a positive trend in the frequency and duration of atmospheric blocking over the Barents Sea especially in winter, supporting the statement of an enhanced North Atlantic pathway for meridional transport.

MWAIs frequently transport transport large amounts of heat and moisture into the Arctic through the Atlantic sector (Woods and Caballero, 2016). When the warm air is pushed upwards over cold Arctic air masses, deep cloud systems including mixed–phase clouds may form. During MWAIs, cirrus clouds, whose radiative effect is not well explored over sea ice (Hong and Liu, 2015; , can be formed or advected to the ArcticOver the past decades, the frequency of meridional transports through the North Atlantic has increased due to more frequent atmospheric blocking over the Barents Sea (Mewes and Jacobi, 2019; You et al., 2022) . Woods et al. (2013) and Woods and Caballero (2016) stress found that intense MWAIs may have a large effect on the downward terrestrial thermal-infrared radiation at the surface, contributing to the enhanced warming of the Arctic. Such Furthermore, MWAIs precondition the sea ice for the melting season, resulting in lower sea ice extent at the end of the summer (Kapsch et al., 2013, 2019). Numerical models still struggle to accurately represent the mixed–phase mixed-phase clouds and the transformation processes of the meridionally transported air masses (Pithan et al., 2014; Cohen et al., 2020). MWAIs can often be linked with filamentary bands

MWAIs are often linked with filaments of strong moisture transport, known as Atmospheric Rivers (ARs, Newell et al., 1992). ARs are responsible for over 90 % of the poleward moisture transport across the mid–latitudes mid-latitudes and are frequently accompanied by strong winds and precipitation (Nash et al., 2018). While the precipitation related to ARs can cause snow accumulation during ARs in the Arctic, the enhanced emission of downward terrestrial thermal-infrared radiation by the clouds can lead to melting of snow and sea ice (Neff et al., 2014; Komatsu et al., 2018; Mattingly et al., 2018, 2020; Bresson

et al., 2022; Viceto et al., 2022). In a warming climate, ARs are expected to shift polewards and to intensify due to the increased moisture load (Ma et al., 2020).

~~CAOs~~ Cold air outbreaks (CAOs) are often responsible for severe weather events in the ~~high- and mid-latitudes~~ high- and mid-latitudes and mainly occur in winter and spring (Fletcher et al., 2016; Pithan et al., 2018). ~~Here, we focus on~~ During marine CAOs (MCAOs)~~where~~ , cold and dry air is advected southwards from the sea ice to the ~~ice-free~~ ice-free (open) ocean. Over the open ocean, the strong temperature contrast between the surface and the lower tropospheric air leads to intense fluxes of sensible and latent heat, responsible for 60–80 % of the oceanic heat losses in that region (Papritz and Spengler, 2017). This heat and moisture transfer into the atmosphere destabilizes the atmospheric boundary layer and leads to the formation of cloud streets, which later develop into open ~~cells~~cloud structures. This cloud evolution is ~~not well represented in models but an important feature (Pithan et al., 2018) . MCAOs can also cause the formation of Arctic mesoscale cyclones (Polar Lows, Rasmussen and Turner, 2003; Zahn and von Storch, 2008), which may locally lead to heavy precipitation and strong winds. The formation processes of Polar Lows and their relation to MCAOs are still not fully understood, partly due to the sparsity of measurements in the Arctic (Moreno-Ibáñez et al., 2021).~~ difficult to capture by atmospheric models (Pithan et al., 2018) motivating dedicated measurement campaigns (Geerts et al., 2022; Lloyd et al., 2018).

So far, observations of air mass transformations in the Arctic have mostly been conducted from a fixed local position (Eulerian view). Only a few aircraft based samplings of air mass properties over a limited regional area have been reported (e.g., Wendisch et al., 2019; Mech et al., 2022). To observe air mass ~~transformation processes~~ transformations along their meridional pathway in a Eulerian view, multiple stations that are aligned with the wind direction would be needed. Therefore, Pithan et al. (2018) proposed a ~~quasi-Lagrange~~ quasi-Lagrangian approach following air masses to and from the Arctic~~, which~~ . This motivated the field campaign ~~HALO-(AC)^3~~ HALO-($\mathcal{AC}$)^3 within the Transregional Collaborative Research Center TRR 172 ~~(TRR 172)~~ "Arctic ~~Amplification~~amplification: Climate Relevant Atmospheric and Surface Processes and Feedback Mechanisms ~~(AC)^3~~($\mathcal{AC}$)^3". The campaign was designed to obtain ~~quasi-Lagrange~~ quasi-Lagrangian observational data of air mass transformations during MWAIs and MCAOs to gain process understanding and evaluate the performance of weather and climate models ~~(Wendisch et al., 2021)~~(Wendisch et al., 2021, 2024).

During ~~HALO-(AC)^3~~HALO-($\mathcal{AC}$)^3, extensive remote sensing and in situ measurements of surface, cloud, and thermodynamic properties have been performed between the Norwegian Sea and the North Pole from 11 March to 12 April 2022 ~~with~~ using three research aircraft (HALO, Polar 5, and Polar 6). The High Altitude and LOng-range research aircraft (HALO) operated by the German Aerospace Center ~~(DLR, Ziereis and Gläßer, 2006; Stevens et al., 2019)~~ (Ziereis and Gläßer, 2006; Stevens et al., 2019) is a modified Gulfstream G550~~, which has a sufficient operating range (~~. It has an operating range of 9000 km in altitudes up to 15 km~~) for quasi-Lagrange~~ , which is beneficial for quasi-Lagrangian air mass observations, and was based in Kiruna during ~~HALO-(AC)^3. For HALO-(AC)^3, it~~ HALO-($\mathcal{AC}$)^3. It was equipped with a similar instrumental payload as during the ~~EUREC4A campaign (Stevens et al., 2019; Konow et al., 2021)~~EUREC^{4}A campaign (Stevens et al., 2019, 2021; Konow et al., 2021) . Polar 5 and Polar 6 (P5 and P6) were based in Longyearbyen and operated by the Alfred Wegener Institute, Helmholtz ~~Centre~~ Center for Polar and Marine Research ~~(AWI, Wesche et al., 2016) in a similar coordinated way as during the ACLOUD campaign (Wendisch et al., 2019).~~ (Wesche et al., 2016).

This study ~~focuses on the environmental conditions during HALO-(AC)^3 and their climatological contextto serve~~ aims to investigate whether the atmospheric and sea ice conditions encountered during HALO-($\mathcal{AC}$)^3 were suitable for studying air mass transformation. Herein we analyze which types of air mass transport occurred and how representative the conditions were. Therefore, the conditions are analysed in the climatological context. In this way, our study serves as comprehensive reference ~~in future studies~~ for future studies analyzing the HALO-($\mathcal{AC}$)^3 campaign. After introducing the data ~~basis~~ and methods in Sect. 2, we ~~describe the synoptic development during two dominating periods in Sect. ??. We also provide a view on the conditions at Ny-Ålesund~~ provide a general overview of the weather conditions during HALO-($\mathcal{AC}$)^3 (Sect. ~~??~~), ~~where future studies will use the extensive measurements from the French-German Atmospheric Observatory AWIPEV. Sea ice conditions in the North Atlantic sector of the Arctic are presented in Sect. 6. We further analyse the origin and strength of the MWAIs and ARs~~ 3), which leads to the identification of a warm (Sect. 4) ~~, the conditions during the MCAO periods~~ and a cold period (Sect. 5)~~, the formation and environmental characteristics of the Polar Low (Sect. ??), and Arctic cirrus clouds~~ . Both periods are assessed in the climatological context. For the unusually strong warm phase, we further investigate how the associated precipitation might have influenced sea ice conditions (Sect. ~~??~~), ~~before concluding~~ 6). Finally, we conclude our study in Sect. 7.

2 Data and Methods

2.1 ~~Study domain~~

~~HALO-(AC)^3 flight tracks cover~~ Our study concentrates on the North Atlantic sector of the Arctic, the major pathway of MWAIs (Johansson et al., 2017; You et al., 2022). ~~Based on the flight tracks, we selected three domains for our synoptic analysis as shown in~~ Around the Fram Strait, we define a central region including the marginal sea ice zone (Fig. 1~~. The exact geographical coordinates of the domains are listed in Appendix ??, Table ??. From north to south the domains are referred to as northern region (central Arctic north of Svalbard and Greenland), central region(Fram Strait and Greenland Sea), and southern region (~~) where the air mass transfer from the ocean to the sea ice during MWAIs and vice versa during MCAOs is most pronounced. Within this region, most airborne measurements were performed. To better illustrate how the meridional air mass transition progresses, we also include a southerly domain over ocean including the Greenland and Norwegian Seas between Svalbard and Norway ~~). A particular focus lies on the central region, where measurements were performed with all three aircraft~~and a northerly one in the Central Arctic over sea ice. Note that circulation weather type analysis has shown that the flow in this area is generally meridional, while zonal flow hardly occurs (Schirmacher et al., 2023; von Lerber et al., 2022) .

2.1 Atmospheric ~~conditions observed from HALO and at Ny-~~measurements

Only very few permanent radiosonde stations exist in the Arctic. Therefore, the French–German AWIPEV research base in Ny-Å~~lesund~~

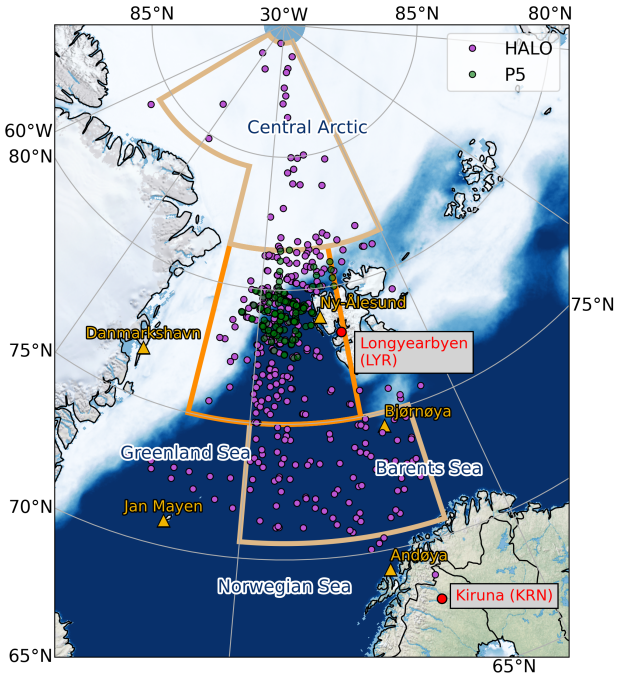

Figure 1. ~~Flight tracks of HALO~~ Study area with corresponding domains (~~purple~~)southern region, ~~as well as P5 and P6 (dark and light green~~central region, ~~zoomed domain in the right panel~~and northern region) ~~during HALO–(AC)^3. For orientation, the~~ and mean sea ice concentration ~~from~~ (07 March to 12 April 2022) based on ~~AMSR2~~ satellite data (Spreen et al., 2008)~~is showed as filled contours~~. The ~~three measurement domains~~ locations of the dropsondes launched by HALO (~~southern region, central region, and northern region~~P5) are marked as purple (green) circles. Operational radiosondes stations are indicated by yellow ~~and orange boxes~~triangles.~~The central region is highlighted. The orange label NYA in the zoomed domain marks the location of Ny–Ålesund.~~

~~Vertical~~ lesund (Svalbard), which is the only station within our central domain, plays a key role in observing atmospheric conditions in the region. We use the 6-hourly soundings at Ny-Ålesund (Vaisala RS41, Maturilli, 2020b) performed during HALO-($\mathcal{AC}$)^3 to assess vertical profiles of temperature, relative humidity, pressure and wind~~were recorded with RD94 dropsondes launched from HALO (Hock and Franklin, 1999; George et al., 2021) and radiosondes launched at the Atmospheric Observatory of the French–German AWIPEV research base in Ny–Ålesund (Svalbard)every~~ . Similar in situ profiling data is available from dropsondes (Hock and Franklin, 1999; George et al., 2021) launched by HALO and the Polar aircrafts. In total 330 dropsondes from HALO and 141 from Polar 5 and 6~~hours (Vaisala RS41, Maturilli, 2020b).~~ , distributed over 18 and 13 research flights, respectively, provide profiles in otherwise not sampled areas (Fig. 1).

From the radiosonde profiles, we identified the thermal tropopause according to the WMO definition as the lowest level at which the temperature ~~lapse rate~~ lapse-rate falls below $2\,\mathrm{K\,km^{-1}}$ and does not exceed this value for the next $2\,\mathrm{km}$. The integrated water ~~vapour~~ vapor (IWV) was calculated from profiles of air pressure and specific humidity~~, which was derived from the temperature and relative humidity measurements. Ground based meteorological measurements gathered at AWIPEV~~

. Ground-based meteorological measurements at AWIPEV are available since 1993 and provide an additional view on the environmental conditions during ~~HALO–(AC)^3 in the central region (Maturilli et al., 2013; Maturilli, 2020a). Additionally, we used data from~~ HALO-($\mathcal{AC}$)^3 (Maturilli et al., 2013; Maturilli, 2020a). Here, the CL–51 ceilometer is used to assess the cloud conditions at ~~Ny–~~Ny-Ålesund (Maturilli and Ebell, 2018; Maturilli, 2022). The detection of a cloud base is used to derive the frequency of cloud occurrence on a daily base. Long-term precipitation observations are performed manually by the Norwegian Meteorological Institute (MET Norway). For Ny-Ålesund (station number SN99910), daily precipitation totals (06 to 06 UTC) are available since 01 January 1974 and have been analyzed in this study for March and April of the years 1974 to 2022.

2.2 Satellite observations of sea ice

~~We focused on sea~~ Sea ice concentration (SIC), i.e., the percentage of a satellite pixel ~~(grid cell in ERA5)~~ covered by sea ice, ~~derived from satellite measurements to describe the sea ice conditions during HALO–(AC)^3. In general, we separated observations for areas with and without sea ice (latter is also termed open water) through the threshold of 15 % SIC. Satellite based passive microwave radiometers provide a long–term observation of sea ice (Spreen and Kern, 2016). Here, we used the OSI SAF~~is obtained from the Ocean and Sea Ice (OSI) Satellite Application Facility (SAF) Global Sea Ice Concentration Climate Data Record (SIC CDR v2.0), namely the product OSI–450 from 1979 to 2015, and the complementary Interim Climate Data Record OSI–430–b from 2016 onwards (OSI SAF, 2017; Copernicus Climate Change Service (C3S), 2020). The product is based on ~~low–frequency~~ low-frequency passive microwave satellite data and is described in Lavergne et al. (2019). The datasets are available ~~daily~~ on a daily basis with a grid spacing of 25 km × 25 km.

~~To study the evolution of SIC during HALO–(AC)^3 at~~ For a higher spatial resolution ~~, we used the merged MODIS–AMSR2 SIC dataset, available daily at~~ (1 ~~resolution. The~~ km), i.e., for the analysis of how SIC changed during HALO-($\mathcal{AC}$)^3, the merged MODIS–AMSR2 ~~product (Ludwig et al., 2020) takes advantage of the high spatial resolution of thermal infrared (Drüe and Heinemann, 2004), and of the independence of cloud cover of microwaves (Spreen et al., 2008)~~SIC product (Ludwig et al., 2020) is used.

2.3 Reanalysis data and diagnostics

~~To analyse the weather development, we used the ERA5 reanalysis from the~~ The European Centre for ~~Medium–Range~~ Medium-Range Weather Forecasts (ECMWF) ~~.~~ reanalysis ERA5 (Hersbach et al., 2018a, b, 2020) offers hourly data output since 1950 with a horizontal resolution of 31 km and 137 vertical model levels~~(Hersbach et al., 2018a, b, 2020). ERA5 represents clouds and precipitation in the Arctic better than other reanalyses (Graham et al., 2019a; Avila-Diaz et al., 2021). Additionally~~. For our region, ERA5 ~~features a higher vertical resolution than other reanalyses, which leads to more accurate wind fields and, thus, to improved water vapour transport estimates (Graham et al., 2019b). However, ERA5 shows higher warm biases over sea ice of near surface temperatures than other reanalyses due to the misrepresentation of~~ has been found superior compared to other global reanalysis (Graham et al., 2019a, b; Avila-Diaz et al., 2021). With very few ground-based stations in our study area, the ~~stable stratification (Wang et al., 2019; Yu et al., 2021). During HALO–(AC)^3, dropsonde measurements launched from HALO were assimilated into~~ assimilation of satellite data plays a major role for the quality of ERA5. ~~The climatological comparisons~~

~~presented here are based on~~ Therefore, our climatological analysis uses the years 1979–2022 ~~unless specified differently. Grid points with a land fraction > 0 have been excluded from our analysis according to the ERA5 land–sea–mask.~~ starting with the onset of the satellite era. Note that during HALO-$(\mathcal{AC})^3$, 216 dropsondes were used in the Global Telecommunication System data assimilation, likely resulting in an improved reanalysis quality.

Domain averages of the regularly gridded ERA5 ~~quantities~~ data were calculated as area averages weighted by the cosine of the latitude to respect the increasing data point density with increasing latitudes. ~~In the following, we describe the processing of ERA5 data and derivation of indices calculated for~~ Grid points with a land fraction > 0 have been excluded from our analysis. ERA5 data serve to detect MWAI, ARs, and MCAOs:

2.3.1 ~~Detection of Atmospheric Rivers and moist and warm air intrusions~~

~~Woods and Caballero (2016) detect moist air intrusions into the Arctic when the~~

- **MWAIs** are identified by positive daily means of the vertically integrated meridional moisture flux ($\mathrm{IVT_{north}}$) ~~at 70° N exceeds 200 $\mathrm{Tg\,d^{-1}\,deg^{-1}}$ (60.6 $\mathrm{kg\,m^{-1}\,s^{-1}}$) over a duration of at least 1.5 days and a zonal extent of at least 9°. For our purpose, we adapted this detection and defined MWAIs with positive daily means of $\mathrm{IVT_{north}}$~~ averaged over the central region. ~~An~~ Guided by the study of Woods and Caballero (2016) an MWAI is considered weak (strong) when $\mathrm{IVT_{north}}$ is below (equal or above) 100 $\mathrm{kg\,m^{-1}\,s^{-1}}$. ~~Additionally, we computed the temporal mean, 25–75$^{\mathrm{th}}$ and 10–90$^{\mathrm{th}}$ percentiles over the climatology period. In this study, ARs were identified with a global algorithm by~~

- **ARs** are detected by the global algorithm from Guan and Waliser (2015) in its revised version (Guan et al., 2018), adapted to the lower moisture content of the Arctic ~~(Lauer et al., 2023b).~~ by reducing moisture transport thresholds. Data set in one-hour resolution is available at Lauer et al. (2023a).

2.3.1 ~~Marine cold air outbreak index~~

~~A key feature of MCAOs are strong temperature decreases~~

- **MCAOs** are characterized by their strong temperature decrease with increasing height ~~especially in the lower troposphere over~~ over the open ocean. ~~This forms the basis for the MCAO index M to identify them and to quantify their strength.~~ The MCAO index M ~~was~~ is calculated following Papritz and Spengler (2017) and Dahlke et al. (2022):

$$M = \theta_{\mathrm{SKT}} - \theta_{850} \tag{1}$$

with θ_{SKT} (θ_{850}) as the potential skin temperature (potential temperature at 850 hPa). Grid points with skin temperatures below 271.5 K (i.e., over sea ice) were excluded from further processing as in Dahlke et al. (2022). ~~We averaged over the central region and computed the climatology as for $\mathrm{IVT_{north}}$.~~ Following Papritz and Spengler (2017), MCAO conditions are present when $M > 0\,\mathrm{K}$ and its strength can be classified as weak ($0\,\mathrm{K} < M \leq 4\,\mathrm{K}$), moderate ($4\,\mathrm{K} < M \leq 8\,\mathrm{K}$), strong ($8\,\mathrm{K} < M \leq 12\,\mathrm{K}$) or very strong ($M > 12\,\mathrm{K}$).

For climatological assessment, we average over each region and compute the temporal mean, 25–75$^{\text{th}}$ and 10–90$^{\text{th}}$ percentiles of $\text{IVT}_{\text{north}}$ and M over the climatology period.

2.3.1 ~~Lower tropospheric parameters for marine cold air outbreak analysis~~

3 Overview of the campaign period

~~For a detailed analysis of the MCAO conditions over the campaign (Sect. 5), we used hourly ERA5 data of wind, temperature, and relative humidity at 850, 925, and 1000 hPa, as well as cloud cover, precipitation and surface turbulent heat fluxes (sensible and latent). All variables were temporally averaged over 6 hour intervals and spatially averaged over the central region. Cloud cover was confined to open water surfaces only as ERA5 tends to overestimate especially low–level cloud cover over sea ice (Di Biagio et al., 2021). Details can be found in Appendix ??.~~

3.1 Ny-Ålesund

3.1.1 ~~Environmental conditions of Polar Lows~~

~~We analyse the environment for Polar Low formation with a set of conditions (C1–C6) suggested by Radovan et al. (2019) and Terpstra et al. (2016) in a 200~~Radiosoundings from Ny-Ålesund provide the only continuous source of information on the vertical structure of the atmosphere in our study region and are therefore frequently used to characterize the climate of the whole North Atlantic sector of the Arctic (Maturilli et al., 2013). The temperature and moisture profiles measured by radiosondes at Ny-Ålesund during the HALO-$(\mathcal{AC})^3$ are shown in Fig. 2 and indicate a high temporal variability at all altitudes. Temperatures near the surface (5 km) vary between $-20\,^{\circ}\text{C}$ and $+5\,^{\circ}\text{C}$ ($-45\,^{\circ}\text{C}$ and $-20\,^{\circ}\text{C}$), indicating the presence of different air masses. This is confirmed by wind measurements, which reveal episodes of strong southerly winds associated with warm temperatures in the first half of the campaign, while in the second half of the campaign weaker, mainly northerly winds associated with lower temperatures prevail. The strongest episode of warm air advection on 12–13 March led to an increase of 2 m temperature from about $-14\,^{\circ}\text{C}$ to $+2\,^{\circ}\text{C}$ within 19 hours (meteorological tower measurements, not shown). This air mass lifted the tropopause up to 13 km ~~radius around the Polar Low's centre (pressure minimum): C1: sea surface temperature (SST) — 500 temperature, C2: SST —~~ (Fig. 2a), and the 2 ~~temperature, C3: mean lapse rate below 850, C4$_{\text{i}}$: mean relative humidity below 950, C4$_{\text{ii}}$: mean relative humidity between 850 and 950, C5:~~ m temperature remained above freezing for five days. The 2 m temperature even reached a new maximum for March on 15 March (5.5 °C) since the beginning of the data record in 1993.

To investigate whether the observed warm air advection was related to ARs we analyze humidity profiles. The first half of the campaign featured a number of short-term events of high integrated water vapor (IWV) as shown in Fig. 2b. On 15 March, a radiosonde measured an IWV of $14.6\,\text{kg}\,\text{m}^{-2}$, which is the highest value recorded between 07 March and 12 April from 1993 to 2022. The rapid doubling of IWV within a day already gives an indication of the presence of ARs. Applying the detection algorithm to reanalysis (Sect. 2) confirms that two ARs passed over Ny-Ålesund. AR I arrived at Ny-Ålesund on 12 March at 13 UTC and lasted until 14 March, 13 UTC. However, in the AR detection algorithm this AR consisted of two parts with

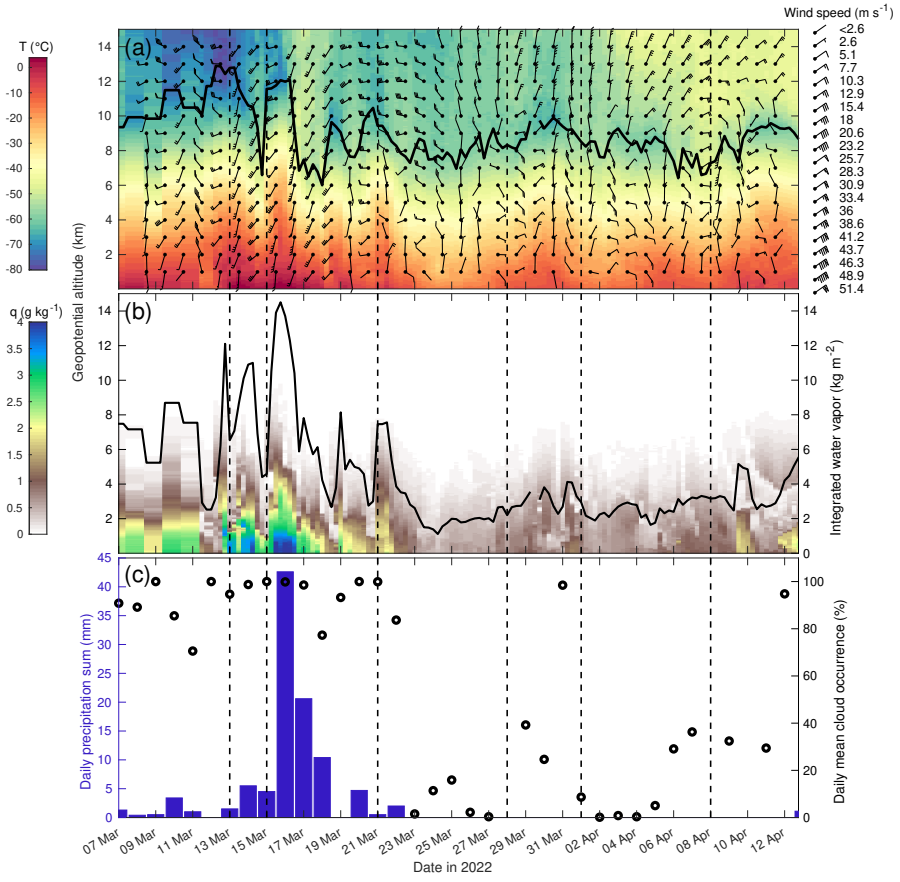

Figure 2. Time series of Ny-Ålesund radiosondes of (a) temperature profiles (shading), height of thermal tropopause (black line), and wind barbs in selected levels, (b) specific humidity profiles (shading) and resulting IWV (black line, right axis). (c) shows daily accumulated precipitation (06 to 06 UTC) from gauge measurements and daily mean cloud occurrence from ceilometer measurements.

enhanced moisture transport and IWV, which can also be seen in the IWV dip on 13 March between two peaks (12 and 14 March) in Fig. 2b. AR II reached Ny-Ålesund on 15 March at 03 UTC and was only detected until 22 UTC of the same day although IWV and the moisture transport stayed on high levels until 16 March, 15 UTC (not shown).

The second half of the campaign was drier, featuring the lowest IWV of less than $1.2\,\mathrm{kg\,m^{-2}}$ on 24 March at 06 UTC. This IWV is below the 3rd percentile of all radiosondes between 07 March and 12 April from 1993 to 2022 (Maturilli and Kayser, 2016, 2017; Ma

. Afterwards, IWV varied less and stayed below $4\,\mathrm{kg\,m^{-2}}$ throughout the second half of the campaign. Only on 10 ~~wind speed (here, gust), C6: 500 geopotential height anomaly. Condition C3 is evaluated as the vertical mean of the vertical potential temperature gradient between the surface and the 850 pressure level. The meaning of each condition is summarized in Appendix ??.~~ April, enhanced moisture values indicate a weak moist air advection that was relevant for the formation of cirrus clouds over sea ice observed by HALO (not shown).

For conditions C1–C4, The ceilometer at Ny-Ålesund reveals high cloud occurrence until 23 March (Fig. 2c). The high cloudiness is accompanied by precipitation and related to the MWAIs and ARs passing over Ny-Ålesund. From 15 March, 06 UTC to 16 March, 06 UTC, 42 mm of precipitation was recorded, which is the highest daily accumulated precipitation for March since the beginning of the measurements. The situation changed during the course of 17 March, when the cloud deck started to dissolve, and the 75th percentile, for C5, the maximum, and for C6, the mean were computed. Wahl et al. (2017) found that scales of multiples of the grid cell spacing are required to realistically represent the energy spectrum of 2 m temperature dropped below 0 °C. No further precipitation was observed after 23 March, and cloud occurrence generally remained low at Ny-Ålesund until the end of the campaign. However, note that Ny-Ålesund is located within a wind field. We decided to use the maximum fjord on the west coast of Svalbard and measurements, especially within the atmospheric boundary layer, may be influenced by the local orography (Gierens et al., 2020). For example, the relatively cloud-free second part of the campaign was associated with lee effects.

3.2 Reanalysis

Given the scarcity of measurements, reanalysis data are used to characterize the conditions over the whole study domain. Time series of area-averaged mean sea level pressure (MSLP), 10 m wind gust instead of mean wind to get a better estimate of the near-surface wind field of this small-scale phenomenon that might be hidden due to the coarse resolution of ERA5. The climatology of the wind, 2 m temperature, 850 hPa temperature, and IWV (Fig. 3) illustrate that the major features of warm and moist conditions in mid-March and cooler and drier conditions later on observed at Ny-Ålesund also apply to the central domain. We also look at the spatial distribution of mean sea level pressure, 500 geopotential height for C6 consists of all days of April between 1979 and 2022 for each grid point within the 200 radius. Subsequently, hPa geopotential height and 850 hPa equivalent-potential temperature in the geopotential height anomaly was computed as the difference between the conditions during HALO-(AC)^3 and the climatology, and C6 was obtained by averaging over the 200 circle. North Atlantic sector of the Arctic (Fig. 4) to investigate the driving conditions for synoptic events, such as ARs and MCAOs.

Furthermore, we calculated vorticity from 10 dropsonde measurements taken within 1 hour arranged on a circular pattern. Following Lenschow et al. (2007) and Bony and Stevens (2019), we assumed horizontal variations in the wind field to be linear and expanded the wind vector with Taylor expansion around the centre of the circle in spherical coordinates.

3.2.1 Trajectory calculations

Trajectory calculations were performed using LAGRANTO (Sprenger and Wernli, 2015) and wind fields from ERA5. To assess the origin of sampled cirrus air masses, 72 hour back-trajectories for the northernmost sections of the flights on 11 and The strong warming events observed at Ny-Ålesund between 12 April were computed. Trajectories were initialized at the pressure levels 350–550 hPa in 50 hPa steps, where the single-layer cirrus had been observed by HALO (Sect. **??**) . Furthermore, 72 hour back- and 48 hour forward-trajectories were computed to identify the pathways of the MWAIs (ARs)on 13 and 16 March are related to a low-pressure system over Greenland, which drives southerly winds through the North Atlantic (Fig. 4a). From 13 to 15 March(Appendix **??**). These trajectories were initialized along the 77.5° N latitude with 1° zonal spacing between , the

zonal pressure gradient across the North Atlantic intensifies, leading to stronger southerly winds in all three domains (Fig. 4b, Fig. 3b). In this period, the IWV is very high in the central and northern domains with daily area averages of 12–14 $\mathrm{kg\,m^{-2}}$ and 6–8 $\mathrm{kg\,m^{-2}}$, respectively (Fig. 3e). At the same time, ERA5 indicates 2 m temperatures above freezing in the central domain, which agrees with the time series observed at Ny-Ålesund (Fig. 3c). Around 20 ~~° W and 13° E at 18:00 UTC on the respective days at the pressure levels 700, 850, and 925~~March, the MSLP gradient between the three domains reverses due to changes in the large-scale pressure constellation (Fig. 4c). The central Arctic now shows typical conditions with the highest MSLP of all regions and the strongest static stability as can be judged from the difference between temperatures at 850 hPa ~~,~~and at 2 m (Fig. 3a, c, d). In this second part of the campaign, northerly winds typical for MCAO activity led to extremely dry conditions with IWV down to 1.4 $\mathrm{kg\,m^{-2}}$ in the northern domain (Fig. 3e), clearly indicating a polar air mass.

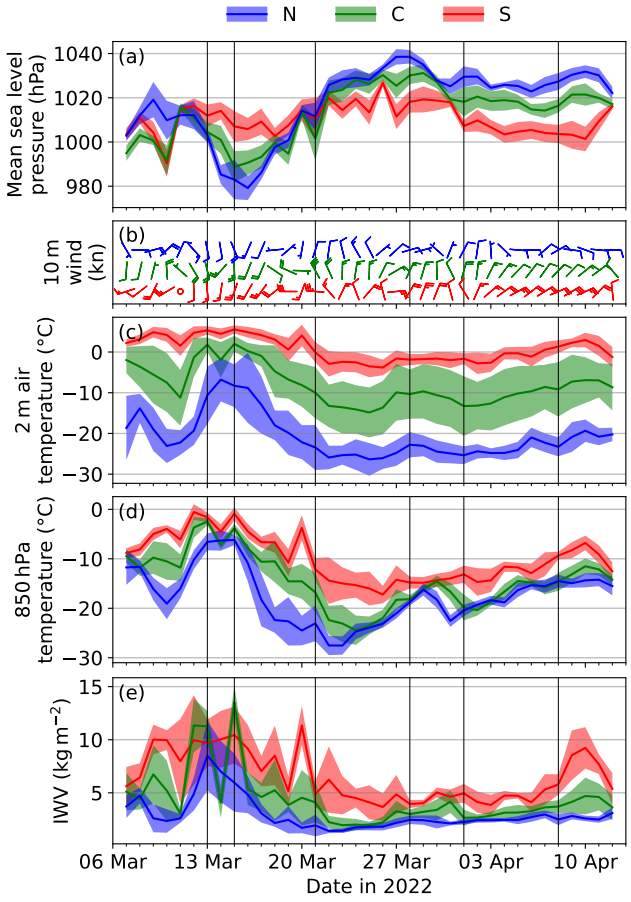

Figure 3. Regional averages (colored lines) and standard deviation (shading) of ERA5-based daily means of (a) mean sea level pressure, (b) 10 m wind speed (wind barbs), (c) 2 m temperature, (d) 850 hPa temperature and (e) integrated water vapor (IWV). Regional averages are performed for the southern (S, red), central (C, green), and northern (N, blue) regions shown in Fig. 1. Vertical black lines indicate days shown in Fig. 4.

4 ~~Meteorological and sea ice conditions during HALO–(AC)^3~~

3.1 ~~Analysis and identification of synoptic events~~

~~In this section, we characterize weather events during HALO–(AC)^3 and assess their strength in the climatological context.~~
~~At first~~ Motivated by the clear differences between the first and second half of the campaign, we separate the campaign into two major periods based on the northward component of the integrated water vapor transport (IVT_{north}) and the MCAO index (M) in the central region (see Fig. 5). ~~The campaign started with a warm and humid period~~with positive ~~IVT_{north}~~ and negative ~~values of M, coinciding with enhanced static stability, from~~ From 11 to 20 ~~March 2022. The warm~~ March, from here on called the warm period~~was followed by a cold and dry period from~~ , IVT_{north} is positive, indicating warm air advection into the Arctic. In the subsequent period (21 March to 12 April~~2022, where~~ , hereafter referred to as cold period), IVT_{north} ~~(M) was almost exclusively negative(positive).~~ turns slightly negative, indicating a moisture flux out of the Arctic. This is connected to MCAO activity as quantified by the positive MCAO index in the cold period. In the following, we assess the weather conditions of warm and cold periods in the climatological context separately.

~~Within the warm and cold periods, we classified a large variety of weather events based on IVT_{north}~~

~~Left column: (a) Calendar of March and April 2022 showing the categorized and colour-coded weather conditions. Bold font indicates days when research flights were performed. Right column: Regional averages (lines) and standard deviation (shading) of ERA5 based time series of (b) mean sea level pressure, (c) 2 temperature, (d) 10 wind (lines indicate speed, barbs indicate direction and speed), (e) integrated water vapour (IWV), and (f) daily accumulated precipitation, separated into rain (no transparency) and snow (partly transparent). Regional averages are performed for the southern (S, red), central (C, green), and northern (N, blue) region shown in Fig. 1. Vertical black lines indicate days shown in Fig. **??**.~~

4 Warm air intrusions

4.0.1 ~~Warm period~~

~~During the warm period, the corresponding~~ To answer what caused the occurrence of the strong MWAIs we analyze the general circulation pattern~~was characterized by a~~ . A high surface pressure system ~~extending from the North Sea to Baltic Sea and Scandinavia (Fig. **??**a, b). The surface high~~ over Scandinavia was connected to a ridge in the 500 hPa geopotential height~~. Low surface pressure and low 500~~, resulting in a blocking situation (Fig. 4a, b). The blocking is evident in Fig. 6b, showing the strong anomalies of more than 10 hPa ~~geopotential height were located over Greenland and the North Atlantic. This pressure constellation resulted in a consistent southerly and southwesterly flow with only a few short–lived interruptions in the three measurement regions. The interruptions can be seen as near–surface temperature drops and wind direction change (e.g., 11 March, Fig. **??**c, d).~~

~~On 11–13 and 15–16 March, the pressure gradients between Greenland and Scandinavia were intensified and blocking (Omega Block) was established over most of Europe~~in the MSLP field over the whole warm period with lower pressure over

Greenland and the central Arctic, and higher pressure over Scandinavia. Intense MWAIs are often connected to blocking situations over the eastern border of a large basin (here, North Atlantic), redirecting cyclones northward as the typical eastward propagation is blocked (Woods et al., 2013). Consequently, warm and moist air masses originating from the North Atlantic were transported towards ~~our three main measurement areas~~the Fram Strait, driven by several ~~low pressure~~ low-pressure systems that formed between Iceland and eastern Greenland.

~~We identified a strong MWAI event during the first week of the campaign~~ All days of the warm period passed the criteria for MWAI occurrence (Sect. 2), and from 12 to 17 March, IVT_{north} exceeded the 90th percentile of the ERA5 climatology on each day (Fig. ~~??a)with area-averaged IVT_{north} up to 160 kg m^{-1} s^{-1}~~ 5a).

Not surprisingly, temperatures at 2 m and 850 hPa show positive anomalies over all domains during the warm period (Fig. 6e, h). However, with far above 8 K, the strongest 2 m temperature anomalies occur over sea ice surfaces. Together with the weaker positive anomaly at 850 hPa (up to 7 K in the three domains), this demonstrates the decreased stability of the lower atmosphere during this period over sea ice. The warm period was also moister than average as indicated by the positive IWV anomalies over all domains (Fig. ~~5a). The event was detected as AR and~~ 6k). Note that although the highest IWV anomalies occurred in the southern region, the relative effect increases with higher latitudes as IWV mean values generally decline towards the North along with the decreasing temperatures. The highest relative IWV anomalies (up to 90 %) occurred over sea ice northwest and northeast of Svalbard (not shown). Note that this latitudinal effect also makes it difficult to diagnose ARs based on IWV only.

The two AR events detected at Ny-Ålesund also affected the entire measurement area of HALO-$(AC)^3$. However, the timing might be different, depending on the exact location. AR I passed through the measurement regions on ~~12–13~~ 12–14 March (Fig. ~~??~~2b and Fig. 4a). In the northern ~~region~~domain, IWV reached its campaign maximum (8 kg m^{-2}) on 13 March and declined afterwards while the 850 hPa and 2 m temperature in the northern ~~region~~ domain continued to increase until the following day (Fig. ~~??d, e).~~

~~A second AR followed~~ 3c–e). AR II, which arrived on 15 ~~and 16~~ March (Fig. ~~??a), which had a more distinct confluent tropospheric southwesterly flow between the Greenland low and the Scandinavian high~~ 4b), had slightly less IWV over the central domain (Fig. ~~??b). In the central Arctic Ocean, the strongest warming occurred on 16 March and resulted in the highest 2 m temperature in March averaged over all ERA5 grid points north of 80° N (latitude-weighted) since 1979 (not shown). Simultaneously, the latitude-averaged IHT_{north} and IVT_{north} exceeded the previous maxima from 1996 ($9.44 \cdot 10^{10}$ W m^{-1} vs. $9.32 \cdot 10^{10}$ W m^{-1}, and 388~~3e). This shows that Ny-Ålesund is not representative of the whole region because here, AR II had the highest IWV. The strong northward moisture transport related to these ARs can be seen in area averages of IVT_{north}, which reached 225 kg m^{-1} s^{-1} ~~vs. 384 kg m^{-1} s^{-1}, Fig. ??). In some parts of the northern region, near-surface temperatures were above freezing and even liquid precipitation was documented over the sea ice (Fig. ??e, f, analysed in greater detail in Sect. 4). The AR on 15–16 March also caused the highest daily precipitation of the northern region over the campaign period. In the central region, the area-averaged 2 m temperature was above freezing and a high fraction of rainfall to the total daily precipitation was found.~~ due to AR II in the central domain (Fig. 5a).

~~After the AR, much drier but still relatively warm air followed, leading to a strong reduction in IVT_{north} and a slight reduction in IHT_{north} (Fig. ??). As a surface based high pressure system formed over Greenland, the large-scale pressure~~

~~constellation started to change. However, at upper levels, low geopotential persisted, promoting the formation of a strong low pressure system near Iceland on 20 March. The low quickly propagated towards the northeast and was characterized by rapid deepening ($>25\,\mathrm{hPa}$ core pressure decrease in 24 hours) and a frontal structure representative of a Shapiro–Keyser cyclone (Shapiro and Keyser, 1990). On the eastern flank of the Shapiro–Keyser cyclone, $\mathrm{IHT}_{\mathrm{north}}$ and $\mathrm{IVT}_{\mathrm{north}}$ indicate similarly strong fluxes as on 12 March~~

We compare the strength of the ARs during HALO-$(\mathcal{AC})^3$ to the long-term climatology in Fig. 7. For this purpose, the mean IVT over the detected AR area and the AR's central latitude are shown in relation for all six-hourly ERA5 time steps since 1979. Note that a slightly different region over the North Atlantic and the Arctic Ocean was selected to extend the view southwards to cover the major pathways of ARs (Guan and Waliser, 2017; Nash et al., 2018). Along their northward propagation, ARs generally decline in intensity. If ARs start to form in the Arctic, their moisture supply is already reduced so that their intensification is limited (Papritz et al., 2021). Therefore the number of strong AR events decreases meridionally (Fig. ~~??~~7).

~~In the climatological perspective, the prevailing pressure gradient between Scandinavia and Greenland is reflected in the extremely strong gradient of the $500\,\mathrm{hPa}$ geopotential height anomalies (>10 over Scandinavia, <-10 over Greenland, Fig. 6h)and was responsible for the associated warming. Moreover, we found positive temperature anomalies at $850\,\mathrm{hPa}$ of more than $7\,\mathrm{K}$ over the Fram Strait and up to $9\,\mathrm{K}$ over Scandinavia and around Franz Josef Land (northeast of Svalbard, Fig. 6b). At $2\,\mathrm{m}$, the warming was amplified to more than $16\,\mathrm{K}$ above climatology over Franz Josef Land and more than $10\,\mathrm{K}$ over the Greenland Sea and Fram Strait~~

AR I and AR II both represent strong cases in terms of mean IVT as they partly lie outside the 25$^{\mathrm{th}}$ percentile in latitude–IVT space (Fig. 7). At its northernmost position with a central latitude of 80° N, AR I had a stronger mean IVT than 90 % of all ARs in the climatology. However, AR II was characterized by even stronger moisture transport but did not reach as far north as AR I. When AR II was at its northernmost position (centered at 76° N), its area-averaged IVT was just below $200\,\mathrm{kg\,m^{-1}\,s^{-1}}$ and therefore also higher than 90 % of all ARs in the climatology (Fig. ~~6c~~7). The ~~bottom–amplified warming is consistent to the findings of Woods and Caballero (2016), confirming the reduction of the Arctic boundary layer inversion strength through intense MWAIs. Additionally, the high amounts of moisture carried by the ARs resulted in positive IWV anomalies of more than $2\,\mathrm{kg\,m^{-2}}$ over the southern, central , and parts of the northern region (up to $4\,\mathrm{kg\,m^{-2}}$ in the Norwegian and Greenland Seas, Fig. 6k).~~

~~Maps of mean sea level pressure (white contour lines), 500 geopotential height (black contour lines), and 850 equivalent–potential temperature (shading and grey contours) from ERA5 data for representative days of the main weather conditions at 12 UTC. 13 March (a) and 15 March (b) represent the moist and warm air intrusions with AR characteristics, (c) shows the Shapiro–Keyser cyclone on 21 March that marked the beginning of the cold air outbreak period, 28 March (d) and 01 April (e) represent the persistent northeasterlies with varying cold air advection strength, and (f) features the Polar Low west of Svalbard on 08 April. The 15 % sea ice concentration from AMSR2 (Spreen et al., 2008) is displayed as blue contour line.~~

~~Hovmöller diagram of hourly vertically integrated meridional fluxes of (a) heat ($\mathrm{IHT}_{\mathrm{north}}$), and (b) moisture ($\mathrm{IVT}_{\mathrm{north}}$) during HALO–$(\mathrm{AC})^3$, averaged over the central region latitudes. Positive (negative) values indicate northward (southward) fluxes.~~

~~Orange vertical lines indicate the longitude boundaries of the central region. Important synoptic events shown in Fig. ?? are marked by horizontal dashed lines. Data is based on ERA5.~~

4.0.1 ~~Cold period~~

~~On 21 March2022,~~ maximum IVT of AR II (meridional and zonal) slightly exceeded $400\,\mathrm{kg\,m^{-1}\,s^{-1}}$ on 15 March in the ~~Shapiro–Keyser cyclone, together with a strong high pressure system over Greenland, marked a turning point in the circulation pattern (Fig. ??c). Compared to the warm period, the zonal pressure gradient across the North Atlantic has been inverted. The resulting northerly winds caused negative $\mathrm{IHT_{north}}$ and $\mathrm{IVT_{north}}$ after the cyclone passed~~ central region (Fig. ~~??d and ??).~~ ~~Although the sign of the pressure gradient remained until the end of the campaign (12 April), the position and strength of the synoptic– and meso–scale circulations changed over time. As Kolstad et al. (2009) showed, there is a connection between such a circulation pattern and the onset of MCAOs in that region. In all three measurement regions, the area–averaged $2\,\mathrm{m}$ temperature remained below $0\,^{\circ}\mathrm{C}$ until 07 April~~ A1 in Appendix A). HALO's dropsonde measurements showed a maximum IVT of $490\,\mathrm{kg\,m^{-1}\,s^{-1}}$ on 15 March, suggesting that ERA5 underestimates the moisture flux at the local scale. As all AR events had meridionally elongated structures, the outflow region reached far up to the central Arctic while their centers were located at 68–80° N (Fig. ~~??c).~~ 7). During their poleward propagation, the moisture transport decreased so that they no longer fulfilled the detection requirements.

~~As the Shapiro–Keyser cyclone stayed over the Barents Sea while dissipating, IWV dropped to the lowest area–averaged values in the northern region (1.4–$2.4\,\mathrm{kg\,m^{-2}}$, Fig. ??c). Two strong MCAO events were observedduring the cold period. The first one lasted for almost the entire third campaign week with a maximum M of $10\,\mathrm{K}$, which exceeded the 90^{th} percentile of the climatology~~

The northward transport of warm and moist air was associated with anomalous amounts of precipitation (Fig. ~~5b)~~ 8). Particularly when the ARs made landfall in Scandinavia, Svalbard, and eastern Greenland, strong anomalies of up to $8\,\mathrm{mm\,day^{-1}}$ compared to the climatology were observed. The ~~second MCAO event occurred on 01–02 April and exceeded the 75^{th} percentile with M up to $9\,\mathrm{K}$. This event showed the minimum latitude–averaged $\mathrm{IHT_{north}}$ of the campaign ($-5.32 \cdot 10^{10}\,\mathrm{W\,m^{-1}}$, Fig. ??) and did not reach the 0.02^{th} percentile of the climatology.~~

~~Between the two strong MCAO events and after the second one, the MCAO conditions weakened (decreasing M) in the western Fram Strait due to decreasing pressure gradients and calming winds, which turned more towards easterlies (Fig. ??d). Especially in the central region, the near–surface temperature increase (Fig. ??c) indicated the advection of relatively warm air from several subpolar regions across the central Arctic~~ strongest anomalies found on the east coast of Greenland relate to 6 times higher precipitation compared to the climatology. For Svalbard, the ERA5 data are in line with the record-precipitation measured at Ny-Ålesund (Fig. ~~We classified these events as aged warm air periods (Fig. ??a) during which we observed mainly three recurring patterns. First, the easterly winds resulted in cloud–free areas in the lee of Svalbard. Second, converging winds over the central Fram Strait led to increased convective cloud formation. Third, some cloud streets developed over~~ 2) coming from AR II. The area of increased precipitation reaches up to the ~~western Fram Strait due to a less disturbed off–ice flow. Both position and intensity of these patterns varied from day to day. On 05–06 April, the relatively warm air was still present in~~

the measurement regions , but the advection was weaker due to reduced horizontal pressure gradients. Therefore, we did not attribute these days to one of the weather classes defined in Fig. **??**. North Pole, where precipitation is enhanced by more than a factor of 2.

On 07 April, another weak MCAO (Fig. 5b) and the positive vorticity of an upper–level trough reaching Fram Strait promoted the formation of a mesoscale cyclone with features of a Polar Low (Fig. **??**f, details in Sect. **??**). In the following two days, the Polar Low moved to the northwest and dissipated over the sea ice northeast of Greenland. In parallel, a low pressure complex over Scandinavia advected warm and moist air from Siberia towards the Norwegian Sea. This air mass caused an increase of IWV above $10\,\mathrm{kg\,m^{-2}}$ over parts of the southern region (Fig. **??**c) and was advected northwards with a southerly upper–level flow in the following days (10–12 April). The elevated moist air led to the formation of cirrus clouds over the western Fram Strait (see Sect. **??**). The phase of the precipitation is highly important for its climate effect, and the transition of Arctic precipitation from snowfall to rain is heavily discussed (Serreze et al., 2021). While we note the difficulties of correctly differentiating precipitation phase, it is important to note that northwest of Svalbard, ERA5 showed record-breaking rainfall connected with near surface temperatures above zero. Liquid precipitation at high latitudes over sea ice was also observed by the cloud radar onboard HALO as we detected a distinct bright band at about 0.5–1 km height during research flights. Thus, the observations confirm the presence of liquid precipitation at least in some regions over sea ice. This motivated us to examine the impact of this AR on the sea ice later on (Sect. 6).

Overall, the period of pronounced MCAO activity lasting

In summary, the warm period observed during HALO-$(\mathcal{AC})^3$ featured ARs with averaged IVT values higher than 90 % of all ARs in the climatology. This transport was related to a blocking event affecting the Arctic up to the North Pole with heat and anomalously high precipitation, including record-breaking rainfall rates over the sea ice northwest of Svalbard.

5 Cold air outbreaks

The warm period was followed by a cold and dry period from 21 March to 12 April much better reflects the typical state of the central region than the preceeding warm period. Climatologically, the entire campaignperiod is characterized by weak MCAO conditions until the end of the campaign, where $\mathrm{IVT}_{\mathrm{north}}$ (M between 1 and 3 K) . With a duration of 5–6 days, the first HALO–$(\mathrm{AC})^3$ MCAO period (21–26 March) was slightly longer than the mean duration of MCAO events (3–4 days, Terpstra et al., 2021) . During the cold period, the 500 hPa geopotential height anomalies were negative over Scandinavia and northwestern Russia (coinciding with low surface pressure), and positiveover the central Arctic and Greenland (coinciding with high surface pressure, Fig. 6i) was almost exclusively negative (positive) (Fig. 5). The persistence of the northerly winds due to this anomalous pressure constellation explains the longevity of transition from the warm to the MCAO conditions. Negative temperature anomalies at 2 m and at 850 hPa were most prominent in the central Fram Strait, Norwegian Sea and parts of the Greenland Sea, which were affected by the cold air advection cold period was initiated on 21 March, when an intense cyclone centered east of Svalbard began to draw cold air from the central Arctic into the Fram Strait (Fig. 6c, f). Reduced IWV 4c), which caused snowfall on the west coast of Svalbard. In its aftermath, the MSLP anomaly reversed compared to the

climatology overlaps well with the negative 850 hPa temperature anomalies warm period, with positive values in the northwest and negative values in the southeast (Fig. 6l). Positive temperature anomalies at 850 hPa were restricted to regions that were not affected by cold air advection (central Arctic, eastern Barents Sea). Interestingly, the central Arctic Ocean showed negative temperature anomalies at 2 m and positive c). Consequently, the southward flow of cold Arctic air led to cold and dry anomalies at 850 hPa, suggesting enhanced static stability compared to the climatological mean hPa over the open ocean (Fig. 6c, f). This area also shows slightly positive subsidence anomalies at 850 hPa (not shown) . In contrast, the static stability is reduced in the area between Svalbard and Franz Josef Land with positive anomalies at the surface and negative anomalies at 850 hPa. i, l).

5.0.1 Climatological assessment of the full HALO–(AC)^3 period

The 2 m temperature anomalies for the entire HALO–(AC)^3 period (07 March–12 April) were positive in most regions shown in Fig. 6d. Only in the central Fram Strait and north of Greenland negative 2 m temperature anomalies down to −1.2 K and −2.4 K, respectively, were found, coinciding with the regions of strongest negative 2 m temperature anomalies during Within the cold period, two periods of strong MCAO conditions (21–26 March and 01–02 April) were identified whose strength exceeded the 90th (25 March) and 75th (2 April) percentile of the climatology (Fig. 5b). During these strong MCAO conditions, we found the maximum values of turbulent surface sensible and latent heat fluxes, which coincided with the highest wind speeds and lowest temperatures of the cold period . Slightly positive 2 m temperature anomalies over the sea ice in the western Fram Strait indicate that the extremely positive anomalies of $>$ 8 K during the warm period were not completely balanced by negative anomalies during the longer cold period (Fig. 6d–f). Temperature anomalies at 850 hPa were positive in all regions shown in Fig. 6. The strongest anomalies with 2–3.5 K were found over the central Arctic Ocean and northern Barents Sea, coinciding with the regions of positive 850 hPa temperature anomalies during the cold period (Fig. 6a, c). Positive temperature anomalies combined with high surface pressure over Scandinavia (central Arctic) in the warm (cold) periodresulted in overall positive 500 hPa geopotential height anomalies over these regions (not shown). Low-level cloud cover remained high in the central domain until 07 April, reflecting the presence of the convective boundary layer clouds typically associated with MCAOs. Interestingly, while most parameters have reversed anomalies compared to the warm period, precipitation in the central domain also shows a positive anomaly. ERA5 produces an extensive region of enhanced precipitation over open water extending far east and being highest at the Scandinavian coast (Fig. 6g). The lowest 500 hPa geopotential height anomalies were located over the east coast of Greenland, where low geopotential also remained during the first part of the cold period . 8).

Over the central region, we found small northward heat fluxes (IHT_{north} of $5.4 \cdot 10^8$ W m^{-1}) and moisture fluxes (IVT_{north} of 18 kg m^{-1} s^{-1}). Consequently, the thermal energy input into the Arctic through this pathway was slightly positive and the brief but intense MWAIs / ARs overcompensated the long MCAO period. In previous years, IHT_{north} and IVT_{north} were often smaller or even negative over the campaign days and the central region. To compare the MCAOs encountered in the cold period to the climatology we apply a metric established by Knudsen et al. (2018) and characterize each event by its strength and duration in Fig. 9. Herein the duration is defined as the time the MCAO index stays above zero, and the strength is given by its maximum

MCAO index M as indicated in the time series of M in Fig. 9b. Note that we used the central domain for the computation of M while Knudsen et al. (2018) considered a smaller area that lies within our central domain.

Anomaly maps of (a–c) temperature at 850 ($\Delta T_{850\,hPa}$), (d–f) 2 m temperature ($\Delta T_{2\,m}$), (g–i) geopotential height at 500 ($\Delta z_{500\,hPa}$), and (j–l) vertically integrated water vapour (ΔIWV) based on ERA5 for the entire campaign, the warm, and the cold period in the left, middle, and right column. The coloured contours show the long-–term mean subtracted from the mean of the time period in 2022 so that positive (negative) values correspond to anomalies above (below) the long-term mean. The dashed black isolines describe the long—term climatology in each panel. The three measurement regions (shown in Fig. 1) are illustrated as black boxes.

5.1 Ny–Ålesund

The extensive remote sensing observations at Ny-Ålesund may complement the airborne observations during HALO-(AC)^3. However, Ny-Ålesund is located at the eastern edge of the central region and measurements may be influenced by the local orography. Based on the temperature profiles The statistics over the long-term ERA5 climatology (Fig. 2a) , the atmospheric conditions at Ny–Ålesund can also be divided into a warm (11–21 March)and a colder period (22 March–12 April). Compared to the full central region, this indicates a temporal shift of one day.

The warm air advection related to the first AR led to an increase of 2 m temperature from about $-14\,^{\circ}C$ to $+2\,^{\circ}C$ within 19 hours (meteorological tower measurements, not shown). Vertical advection of heat and moisture lifted the tropopause to 12.9 km (measured by the 12 UTC radiosonde on 12 March , Fig. 2a). The 2 m temperature remained above freezing for five days9a) generally show that longer MCAO events are also more intense (higher peak M). During the HALO-(AC)^3 period, distinct MCAO events could be identified, separated by short phases with $M < 0$ K visible in high temporal resolution only. The first and even reached a new maximum for March on 15 March (5.5 °C). On this day, also the highest IWV was observed (14.5 kg m^{-2}, Fig. 2b).

The warm period was characterized by constant low–level cloud cover over Ny–Ålesund detected by the ceilometer, interrupted only by a few hours of high–level cloud occurrence in connection with a high pressure ridge passing the site in the night of 14–15 March (not shown) . The situation changed during the course of 17 March, when the cloud deck started to dissolve and third event, starting on 18 March and 11 April, respectively, were relatively short-lived (2–3 days) and had a moderate strength (M of about 5 K). Most notably, the 2 m temperature dropped below 0 °C.

The influence of second event, which started on 21 March after the passage of the Shapiro–Keyser cyclone (see Sect. **??**) delayed the beginning of the cold period over Svalbard compared to the central region by about one day. Northerly winds corresponding to the MCAO period led to extremely dry conditions with IWV down to 1.1 kg m^{-2} (closest grid point in ERA5 with land–fraction < 0.25: 1.5 kg m^{-2}) on 24 March at 06 UTC (Fig. 2b). This IWV is below the 3rd percentile of all radiosondes between 07 March strong cyclone, was unusually long (19 days) and 12 April 1993–2022 (Maturilli and Kayser, 2016, 2017; M . At Ny–Ålesund, the MCAO conditions on 23–30 March, and on 01–05 April were mostly associated with clear sky and 2 m temperatures below $-12\,^{\circ}C$. Aged warm air reached Ny–Ålesund on 28–29 March with more humidity, with slightly higher

~~temperatures and IWV increasing to 4 kg m^{-2}~~had a maximum M of about 11 K. Since 1979, only 9 of the 179 events over the HALO-$(AC)^3$ period had a longer duration. Analyzing the time series with hourly resolution (Fig.

~~Especially during the cold period, cloud conditions at Ny-Ålesund are not representative for the central region because of lee effects as visible on MODIS images~~ 9b), the 21 March MCAO event consists of multiple waves of strong MCAO conditions (pulses of stronger transport) that weakened over time. The most intense MCAO conditions were related to the presence of cyclones near Svalbard, which influenced the atmosphere over the Fram Strait (e.g., ~~NASA Worldview, not shown). Additionally, the temporal delay related to the propagation of synoptic systems during the warm period must be kept in mind when combining Ny-Ålesund with HALO-(AC)^3 observations~~Fig. 4c, e, f). Lower tropospheric winds were stronger and more northerly during the stronger MCAOs. When the cyclones dissipated or propagated away from the area, winds were weaker, and the MCAO strength decreased (e.g., Fig. 4d).

5.1 ~~Sea ice conditions~~

6 Effect of MWAI on sea ice conditions

The different ~~synoptic patterns~~ atmospheric conditions likely affected the sea ice conditions in the measurement ~~areas. In Fig. 10a–c, we present~~ area. To understand the impact on sea ice, we examine the spatial distribution of SIC before (09–11 March) and during (14–16 March) the MWAIs and ARs, as well as after the MCAO period (10–12 April) as shown in Fig. 10a–c. SIC was $> 90\,\%$ in almost the entire northern region in the first period (Fig. 10a). In the central region, the sea ice covered 30–40 % of the area with a southwest–northeast oriented edge. The southern region was almost completely ~~ice-free~~ ice-free over the entire campaign duration (Fig. 10a–c). ~~A time series of SIC for the central region compared to the climatology is shown in Fig. 10d.~~

The ~~MWAI / AR events on 12–13 and 15 March~~ MWAIs and ARs caused a reduction of SIC in the northwestern part of the central region, resulting in the lowest SIC values of the entire campaign period (Fig. 10b, d). ~~SIC~~ While the main sea ice boundary stayed at the same location, the SIC in the marginal ice zone declined. SIC was below the climatological mean but remained within the 10–90$^{\text{th}}$ percentiles. Furthermore, an unusually large polynya opened from north of Svalbard to Franz Josef Land, which resulted in the ~~below-average static stability~~ below-average static stability and stronger turbulent surface heat fluxes during the cold period in this region (Fig. 10b). We assume that ice dynamics related to strong winds caused the SIC decrease in the central region, but ice melt cannot be excluded as well because temperatures were above freezing, and liquid precipitation was observed over sea ice ~~.~~ (Sect. 4). Rapid ice melt has been attributed to warm air advections and induced increases of heat flux in summer (Tjernström et al., 2015; Woods and Caballero, 2016). ~~Although the liquid~~ Liquid precipitation on snow alters the signal of the microwave radiometry and ~~might have increased~~ increases the uncertainty of ~~the SIC product (Stroeve et al., 2022; Rückert et al., 2023), that~~ SIC products (Stroeve et al., 2022; Rückert et al., 2023). However, SIC reduction was obvious in visual satellite images as well (e.g., NASA Worldview, not shown). After the ~~AR events~~MWAIs, the sea ice conditions recovered ~~and the polynya closed again~~ as temperatures fell below the freezing point and northerly winds were established during the MCAOs (Fig. 10c, d). The polynya was also closed again, mostly due to sea ice transport from the

central Arctic. ~~This southward transport can be attributed to the winds during the high MCAO activity between 21 March and 07 April.~~

~~For most of the campaign period, the average SIC in the central region was~~ With respect to the long-term climatology, SIC during HALO-$(AC)^3$ was mostly above the climatological mean in our central domain (Fig. 10d). ~~A map of SIC anomalies compared to the climatological mean is illustrated in Fig. 10e. Southwest of 75° N and 0° E as well as northeast and southeast of Svalbard, SIC anomalies were negative. In contrast, a~~ The positive SIC anomaly was ~~found in the central and western Fram Strait~~related to a further east expansion of the sea ice off Greenland, which overlaps well with the negative 2 m temperature anomalies shown in Fig. 6d, f. ~~The~~ In contrast, the west coast of Svalbard used to be covered by ice in the climatology but was completely ~~ice–free during HALO–(AC)^3. In the northern and southern regions, the mean SIC for the entire campaign period did not differ more than 5 % from the climatological mean~~ice-free during HALO-$(AC)^3$. Similarly, southwest of 75° N and 0° E, as well as northeast and southeast of Svalbard, SIC anomalies were negative (Fig. 10e) in line with the strongest warm anomalies of the campaign.

Note that uncertainties of derived SIC in the marginal ice zone are especially large ~~due to weather related filters and~~ as a result of temporal and spatial ~~interpolations.~~ interpolation (smearing uncertainty), and due to so-called weather filters. Weather filters remove the atmospheric contribution from the satellite signal to remove false sea ice in open-water regions but run the risk of removing true sea ice as well, especially in the MIZ. This mainly affects the central region where the estimated uncertainties of the OSI–SAF SIC product (total standard uncertainty) can reach up to 40 % at the ice edge, mostly due to smearing uncertainty~~(gridding of the swaths, i.e., areas imaged on the surface, from several daily overflights),~~ , and different satellite footprints at different frequency channels.

7 Summary

8 ~~Specific events during HALO–(AC)^3~~

7.1 ~~Warm air intrusions and Atmospheric Rivers~~

~~The warm period was characterized by four independent AR events (12–13 March, 14 March, 15 March, and 20 March) that were at least partly sampled by research aircraft in the three measurement regions. Back trajectory analyses with LAGRANTO (Sect. **??**) revealed that the air masses of the 12–13 March event (Fig. A1a) originated from mid–latitude regions of the North Atlantic and from central Europe (Fig. **??**a). For the second AR event on 15 March (Fig. A1b), the air masses originated almost exclusively from the western part of the mid–latitude North Atlantic (Fig. **??**b). We neglect the ARs on 14 and 20 March as they did not enter the central region, but either propagated northwards to the west of it or dissipated before reaching it. The moist air advection event on 10 April (Fig. **??**c) was too weak to be identified as AR, but was relevant for the formation of cirrus clouds over sea ice~~ In this study, we analyzed the atmospheric and sea ice conditions during the HALO-$(AC)^3$ campaign, whose focus lies on studying transformation processes of air masses on their way into and out of the Arctic.

We compare the strength of AR events during HALO–(AC)^3 by analysing them with respect to the relation between IVT and latitude over the North Atlantic and Arctic Ocean (50–90° N, 60° W–40° E) (Fig. **??**). Note that a different region was selected to extend the view on the North Atlantic, one of the major pathways of ARs (Guan and Waliser, 2017; Nash et al., 2018). Along their northward propagation, ARs generally decline in intensity. If otherwise ARs start to form in the Arctic, their moisture supply is reduced so that their intensification is limited (Papritz et al., 2021). Therefore the number of strong AR events decreases meridionally (Fig. **??**).

North of 70.6° N (southern boundary of the southern region), only few ARs exceed an IVT of $250\,\mathrm{kg\,m^{-1}\,s^{-1}}$ when averaged over the detected AR area (Fig. **??**). In the climatology, the majority has mean values around $150\,\mathrm{kg\,m^{-1}\,s^{-1}}$. The AR events on 12–13, and 15 March represent strong cases in terms of mean IVT for all time steps as they lie outside the 25$^{\mathrm{th}}$ percentile in latitude–IVT space (Fig. **??**). On 15 March at 18 UTC, the AR averaged IVT even exceeded the 10$^{\mathrm{th}}$ percentile while being centered at 76° N. While the AR centre from the event on 12–13 March was located most northerly before it dissipated, the AR from 15 March was characterized by the most intense moisture transport with mean IVT of around $250\,\mathrm{kg\,m^{-1}\,s^{-1}}$ when centered at 70° N, decreasing to $200\,\mathrm{kg\,m^{-1}\,s^{-1}}$ at 75° N. Maximum IVT (meridional and zonal) slightly exceeded $400\,\mathrm{kg\,m^{-1}\,s^{-1}}$ between 13 and 16 March in the central region (see Appendix A, Fig. A1). HALO's dropsonde measurements showed a maximum IVT of $490\,\mathrm{kg\,m^{-1}\,s^{-1}}$ on 15 March, suggesting that ERA5 underestimates the moisture flux. As these AR events had meridionally elongated structures, the outflow region reached up to the central Arcticwhile their centres were located at 70–78° N (Fig. **??**). During their poleward propagation, the moisture transport decreased so that they no longer fulfilled the detection requirements.

The AR events in the warm period were associated with anomalous amounts of precipitation. In Fig. 8, we show the hourly averaged precipitation rate from 11 The campaign took place in the North Atlantic sector of the Arctic from 07 March to 20 March 2022 as well as for the climatology of these days. Along the east coast of Greenland, the total precipitation and snowfall rate partly exceeded $1\,\mathrm{mm\,h^{-1}}$ (Fig. 8a, d), around six times higher compared to climatology (Fig. 8c, f). Over the North Atlantic, Fram Strait, and central Arctic Ocean, total precipitation and snowfall rates exceeded the climatology by a factor of 3. Record breaking rainfall rates were found northwest of Svalbard, exceeding the climatology up to a factor of 36 (Fig. 8i). However, the actual rainfall rate in this areawas below $0.25\,\mathrm{mm\,h^{-1}}$ and the high deviation is caused by even lower rainfall rates in the climatology. Liquid precipitation over sea ice was also observed by the cloud radar onboard HALO during research flights.

In summary, the ARs observed during HALO–(AC)^3 featured uncommonly high AR–averaged IVT values, higher than 90 % of all ARs in the climatology. Additionally, record breaking rainfall rates occurred over the sea ice northwest of Svalbard.

Six hourly climatological (1979–2022) distribution of central latitudes of Atmospheric Rivers (ARs) as a function of mean AR IVT using an ERA5 based AR catalogue modified from Guan and Waliser (2015). Cases categorized as ARs during HALO–(AC)^3 are illustrated by coloured boxes for 06, 12, and 18 UTC of respective flight days. Black (dashed) lines indicate the 25$^{\mathrm{th}}$ and 75$^{\mathrm{th}}$ (10$^{\mathrm{th}}$ and 90$^{\mathrm{th}}$) percentiles of a kernel density estimation to visualize the shape of the histogram. Horizontal dotted lines indicate the latitude boundaries of the three measurement regions (Fig. 1) in the same colours as in Fig. **??**.

Hourly averaged precipitation, snowfall and rain rate ($^{-1}$) derived from ERA5 for (a, d, g) 11–20 March 2022, and (b, e, h) the climatology. In (c, f, i), we show the deviation from the climatology. Note that the rainfall over sea ice is barely visible in both (g) and (h). Positive deviations of precipitation rates are illustrated as the fraction of the average rate in 2022 to the rate of the climatology while negative deviations are given as its inverse.

7.1 Marine cold air outbreaks

The cold period included several MCAO events (21 March–07 April), which are analysed in detail specifically for the central region. Figure **??** shows the time series of atmospheric conditions as described in Sect. **??**. To highlight the conditions in the MCAOs'source region, we also include the temporal evolution of the parameters averaged over the eastern part of the northern region in Appendix **??** (Fig. **??**). The corresponding temporal development over the southern region is shown in Fig. **??** in Appendix **??**.

After the Shapiro–Keyser cyclone, which caused multi–layered clouds and intense snowfall on 21 March at the west coast of Svalbard(Fig. **??**d–g), MCAO conditions were established. From 22 to 26 March, the contribution of convective to total snowfall increased over open water and mid– and high–level cloud cover decreased. Over sea ice, the total snowfall was low and almost exclusively stratiform. Liquid precipitation was not present except for 21 March. Low–level cloud cover remained high until 07 April, reflecting the presence of the atmospheric boundary layer clouds typically associated with MCAOs (Fig. **??**d).

The strong MCAO events (21–26 March and 01–02 April) were characterized by the strongest northerly lower tropospheric winds and high values of domain–averaged turbulent fluxes of sensible and latent heat flux (Fig. **??**a, h). The maximum values of sensible and latent heat coincided with the highest wind speeds and low temperatures (21–22 March, Fig. **??**a, b, h). Note that over the southern region the sensible heat fluxes were slightly lower, whereas, on average, latent heat fluxes were higher than over the central region (Fig. **??**). Near–surface air temperatures increased towards the south, resulting in smaller sensible heat fluxes while latent heat fluxes were increased due to a rising saturation water vapour pressure at the air–sea interface (e.g., Hartmann et al., 1997). We found that larger differences between the specific humidity of the air and specific humidity at saturation in the southern compared to the central region were responsible for the increased latent heat fluxes (not shown).

Temporal evolution of (a) wind, (b) air temperature (T), and (c) relative humidity (RH) on the 1000, 925, and 850 pressure levels, and of (d) low–, (e) mid–, and (f) high–level cloud cover (CC), (g) precipitation, and (h) surface turbulent heat fluxes (STHF, upward is positive) over the central region for 21 March – 07 April 2022 derived from ERA5. For cloud cover, we show the median, the 25 and 75th percentiles, and the 5 and 95th percentiles of a 6 hour interval over open–water surfaces only as crosses, thick vertical lines, and thin vertical lines, respectively. In (g), we display area–averaged values of the accumulated 6 hour snowfall distinguished between convective and total precipitation, and open water (OW) and sea ice (SI). White crosses show the accumulated mean rainfall with more than 0.05 $\mathrm{mm\,(6\,h)^{-1}}$.

During the weak MCAOs and aged warm air periods, northeasterly winds dominated (Fig. **??**a). Compared to strong MCAO conditions, sensible heat fluxes were reduced by a factor of 2 while latent heat fluxes decreased to a lesser extent. Between 27–30 March and 03–05 April, when aged warm air was advected to the central region, precipitation decreased as the air

mass dried and temperatures increased (Fig. **??**b, c, g). Also, foehn effects due to the easterly winds over Svalbard might have contributed to drier and warmer conditions over parts of the Fram Strait as this effect can influence the atmospheric conditions more than 100 off the coast (Shestakova et al., 2022). The eastern parts of the central region close to Svalbard were not fully covered by low–level clouds as the 5 % percentile was mostly between 0.2–0.4. For the first aged warm air period, the southward advection of the air masses from the sea ice covered ocean took about one day. This can be seen when comparing the temporal evolution of the lower tropospheric temperature and relative humidity over the northern and central regions (i.e., low relative humidity from 29 to 30 March, Fig. **??**a–c vs. **??**a–c).

From 05 April on, the mean wind speed decreased and turned to northeast. Hence, more convergent regions developed in the lee of Svalbard with a rather diffuse low–level cloud structure (not shown). These converging winds in combination with a weak MCAO promoted the formation of a Polar Low in the following days, which is explained in greater detail in the next section. Hence, different wind regimes ranging from northwest to northeast and MCAO strengths were observed during HALO–(AC)^3. The large variety of MCAO conditions provides great opportunities for detailed cloud evolution and air mass transformation studies.

7.1 Polar low

The Polar Low formed on 07 April close to the west coast of Svalbard at a baroclinic zone where cold air transported by northeasterly winds converged with warmer North Atlantic air from south to southeasterly winds. During the development phase of the Polar Low, the mean sea level pressure showed closed isobars from 08 12 April 00 UTC on (Fig. **??**f). We examine whether the environmental conditionsC1–C6 (see Sect. **??**) were fulfilled in a 200 km radius around the pressure minimum of the Polar Low at that time (Fig. **??**):

2022. Within this area, we defined three domains over which we investigate whether the conditions were well suited for the campaign's research objectives. The vertical temperature gradient conditions C1 and C2 are fulfilled with 44 K and 8.5 K, respectively, while the lapse rate condition (C3) was not fulfilled with 4.2 K km^{-1}. Conditions C4$_{\mathrm{i}}$ and C4$_{\mathrm{ii}}$, which are a measure for the availability of moisture for latent heat release, exceed the thresholds of 75 % and 82 % with 92.7 % and 93.9 %. Near surface wind gusts reached 16.6 m s^{-1} during the development phase of the Polar Low (00 UTC) and increased to 18.8 m s^{-1} 9 hours later at the mature stage. In both stages, condition C5 was fulfilled. If we considered the maximum of the 10 m wind speed instead of the gust from central domain, which lies in the marginal sea ice zone west of Svalbard, represents the area with the highest research flight activity of the campaign. For our analysis, we relate the conditions during HALO-($\mathcal{AC}$)^3 to the long-term record of Ny-Ålesund measurements, ERA5 , the condition would not have been fulfilled. However, using the Copernicus Arctic Regional Reanalysis (CARRA) from ECMWF with a 2.5 km×2.5 km resolution, we found maximum wind speeds of more than 16 m s^{-1} (19 m s^{-1}) at 00 UTC (09 UTC). The trough connected to the Polar Low was not sufficiently strong with respect to the climatology as the geopotential height anomaly (C6) was only −80 gpm. Anomalously high geopotential around Svalbard and the central Arctic during that time might have obscured the strength of the troughreanalysis, and satellite-derived sea ice conditions.

The radiosonde and surface observations at Ny-Ålesund showed two main periods with different atmospheric conditions. The beginning of the campaign was dominated by extremely warm and moist air masses, resulting in ~~the failure of condition C6.~~

~~Some of the conditions had a large regional variability within the 200 km circle. Condition C2 ranged from below the threshold of 6 K in the southern part of the Polar Low to 10 K in the northern half. As the northwestern part of the circle lay over sea ice, the vertically averaged lower tropospheric lapse rate (C3) indicated stable stratification and reached values up to 10 K km^{-1}. These high values of the lapse rate dominated the computation of the 75th percentile although the lapse rate was below the threshold in most parts of the circle.~~

~~At the mature stage (08 April 06–09 UTC), the region of maximum SST − T$_{500\,hPa}$ difference coincided well with the observed convective clouds during the research flight with HALO in the eastern part of the Polar Low (see Appendix ??, Fig. ??). It also overlapped with the maximum precipitation rate (1.2 mm h^{-1}) and strongest updrafts (-1.75 Pa s^{-1} at 850) indicated by ERA5 (not shown). It is likely that higher precipitation rates and updrafts occurred that were smoothed out by the relatively coarse ERA5 data.~~

~~Dropsonde measurements between 06:55 and 07:53 UTC show high values of relative vorticity in the lowest~~ new maximum 2 ~~km and above 6 km, indicating cyclonic rotation. When averaging ERA5 vorticity over the grid points closest to the dropsonde positions, we find a disagreement to the dropsonde measurementsbelow and good agreement above 4 km height. While the lower tropospheric relative vorticity is related to the Polar Low, the upper tropospheric value is associated with the trough in the geopotential height. The disagreement between ERA5 and the dropsondes could be due to a misrepresentation of the Polar Low's wind field in the reanalysis or due to spatio–temporal mismatches of its position. Measured relative vorticity at 850 hPa (1.5 km height) was about 3.5$\cdot 10^{-5}$ s^{-1} and therefore did not exceed the threshold suggested by Stoll (2022) ($> 20 \cdot 10^{-5}$ s^{-1}). However, the flight track was not perfectly aligned with the Polar Low's centre but extended too far to the south and east where the mean sea level pressure isobars do not suggest a closed circulation (Fig. ??b). Negative relative vorticity to the east of the Polar Low, which is related to lee effects, also influenced the calculation from the dropsonde measurements. ERA5 data shows a maximum of $22 \cdot 10^{-5}$ s^{-1} at 850 hPa within the Polar Low on 08 April at 09 UTC.~~

~~As soon as the Polar Low drifted over sea ice, it started to dissipate due to the loss of atmospheric instability and strongly reduced upward sensible and latent heat fluxes. The Polar Low observed during HALO–(AC)^3 fulfilled four of the six conditions (see Table ??). However, Polar Lows can also form without fulfilling all conditions. Considering the climatology of Polar Lows in Zahn and von Storch (2008), which covers the years 1949–2005, our Polar Low was located unusually far in the north. Also Radovan et al. (2019) investigated 33 Polar Lows with the Arctic System Reanalysis, of which 32 were centered further to the south than our case. Despite its northerly position, the 10 m wind speed of our Polar Low was larger than the average over the 33 Polar Lows investigated in their study.~~

~~Mean sea level pressure (MSLP, white contour lines), 500 geopotential height (black contour lines), and the difference between sea surface temperature (SST) and 500 temperature during the mature stage of the Polar Low on 08 April 2022 06:00 UTC. Additionally, the maximum 10 wind gust at 09:00 UTC (black star and text label) and the HALO flight track (black line with white outline) are included. The Polar Low conditions C1 (SST − 500 hPa temperature), C2 (SST − T$_{2\,m}$), C3 (vertical~~

mean of the vertical potential temperature gradient below 850), C4 (i: mean relative humidity below 950, ii: mean relative humidity between 850 and 950), C5 (maximum 10 m wind speed), and C6 (500 geopotential height anomaly) analysed by Radovan et al. (2019) are given for 08 April 2022 00:00 UTC. Data is based on ERA5.

Criteria to evaluate environmental conditions of a Polar Low in a 200 km radius around its pressure minimum according to Radovan et al. (2019). An "X" in the right column indicates that the condition is fulfilled. Condition Meaning How evaluated Threshold Fulfilled C1 Sea surface temperature − 500 temperature 75th percentile ≥ 43 K X C2 Sea surface temperature − 2 temperature 75th percentile ≥ 6 K X C3 Mean lapse rate below 850 75th percentile $\leq 3\,\mathrm{K\,km^{-1}}$ C4$_i$ Mean relative humidity below 950 75th percentile $\geq 75\,\%$ X C4$_{ii}$ Mean relative humidity between 850 temperatures, record-breaking precipitation and 950 75th percentile $\geq 82\,\%$ X C5 10 wind gust maximum $\geq 15\,\mathrm{m\,s^{-1}}$ X C6 500 geopotential height anomaly mean $\leq -160\,\mathrm{gpm}$

(a) Relative vorticity ζ computed from 10 dropsondes (black) and as model output from ERA5 averaged over the grid points nearest to the dropsondes (blue). (b) Location of the dropsondes (red triangles) launched from HALO while flying in a circle around the Polar Low. ERA5 based mean sea level pressure (white contour lines) and sea ice concentration (coloured filled contours) is shown for 08 April 2022 09 UTC. The HALO flight track is displayed as black line with white outline. Horizontal (horizontal and vertical) hatching indicates areas where ERA5 based 850 hPa relative vorticity is below $-10 \cdot 10^{-5}\,\mathrm{s^{-1}}$ (above $20 \cdot 10^{-5}\,\mathrm{s^{-1}}$).

7.1 Arctic cirrus over sea ice

The sequence of HALO flights between 10 – 12 April aimed to characterize a pronounced field of Arctic cirrus, which entered the central Arctic through the Fram Strait and was finally located close to the North Pole. The initial synoptic state of this period was dominated by a low pressure system, which was centered over Scandinavia on 09 April, advecting integrated water vapor (IWV) for March since the beginning of the measurements. The second half of the campaign was much colder and drier, with mostly clear sky conditions at Ny-Ålesund because of orographic effects. Reanalyses data confirmed these general conditions with northward transport of warm and moist air westwards (see Sect. **??**). Along approximately the 5° W meridian the westward flow converged with a cold air mass that formed over the Greenland ice sheet and flowed eastwards into the Fram Strait. Due to the convergence, a strong vertical wind shear developed south of Greenland with low–level northeasterly winds and southeasterly winds at levels above 700 hPa along the east coast of Greenland. The southerly upper–level flow generated a poleward moisture transport, which was accompanied by cirrus and mid–level clouds west of Svalbard and north of Greenland. This upper–level flow continued during the sequence of three research flights conducted by HALO and roughly connected the air masses sampled during the three consecutive days.

The trajectories of the air masses sampled on 11–12 April are shown in Fig. **??**a, c. While on 11 April two branches, one southerly and one easterly, merged into the area of observations, the trajectories of 12 April first followed the westward moist air transport south of Svalbard and then turned northwards into the central Arctic. Figure **??**b and d illustrate the relative humidity over ice from all dropsondes launched in the central Arctic during the HALO flights on 11–12 April. The mean profile shows an enhanced moisture layer between 4 and 8 . This layer is associated with higher wind speeds up to 25 $^{-1}$ and

a shift in wind direction from an easterly flow in the lower 3 to a southerly flow in the upper troposphere. Below 4 altitude, the air mass was rather dry with relative humidity below 50 %. In these lower altitudes, the stable cold and dry air mass in the central Arctic was supported by the outflow of cold and dry air from northern Greenland and prohibited the formation of clouds below the cirrus. The airborne measurements during this constellation of isolated, widespread cirrus over the sea ice in the central Arctic are well suited to investigate the evolution and radiative effect of Arctic cirrus over sea ice, of which only few observations exist.

(a, c) Three day back trajectories of air masses in which cirrus were sampled on 11 and 12 April 2022. All trajectories are based on ERA5 reanalysis and end at the HALO flight track in cirrus level between 350 and 550. Surface pressure (thin black lines) and cloud cover (black shading) above 550 from ERA5 are shown for 12 UTC at both days. The thick black line indicates the HALO flight track, and red crosses the location of dropsonde releases. In (b, d) we show the average profile and all individual profiles of relative humidity over ice measured during the two flights by dropsondes.

In this study, we described the weather and sea ice conditions during the HALO–(AC)^3 aircraft campaigncarried out from 07 March to 12 April 2022 in the North Atlantic sector of the Arctic. The analysis is based on in the ERA5 reanalysis, dropsondes, satellite based sea ice products, and atmospheric measurements at Ny–Ålesund. We focus on three measurement regions of the campaign: the sea ice covered Arctic Ocean north of Svalbard and Greenland (northern region), first part and a southward flow of cold Arctic air in the Fram Strait (central region), and the Greenland and Norwegian Seas between Svalbard and Scandinavia (southern region). The climatological context is given with respect to the years 1979–2022second part of the campaign.

Based on the vertically integrated meridional water vapour transport (IVT_{north}) and the MCAO index M, the campaign was separated Based on this clear temporal change of conditions, we divided the campaign into a warm period (11–20 March) , and a cold period (21 March–12 April) . and analyzed both in detail.

During the warm (cold) phase, IVT_{north} was positive (negative) while M was negative (positive), respectively.

The warm periodat the beginning of the campaign was characterized by a consistent southerly flow, which led to a strong MWAI on 12–13 March that was detected as an Atmospheric River (AR)and reached the central Arctic. It was followed by an even stronger AR on 15–16 March. Compared to the climatologyperiod, an atmospheric blocking situation diverted cyclones northwards into the Arctic, resulting in strong northward heat and moisture transports (moist and warm air intrusions, MWAIs). Two MWAIs were identified as Atmospheric Rivers (ARs). At their northernmost positions, both ARs denoted higher IVT and were centered further in the north than 75 % (partly, were stronger than 90 %) of all ARs in the North Atlantic pathway within the ERA5 climatology. During the AR on 15–16 March, we found new maxima of vertically integrated meridional heat and water vapour fluxes (IHT_{north} and IVT_{north}) for the central region latitudes. The radiosondes at Ny–Ålesund detected unusually high tropopause altitudes up to 12.9 km. Although the MWAIs were relatively short–lived, they caused a campaign average northward transport of heat and moisture, overcompensating the southward transport of the much longer cold period. We therefore stress the importance of MWAIs for the energy exchange between the mid–latitudes and the Arctic. Averaged over the warm period, new maximum rainfall rates were found over the latitudes of the central domain in the climatology. The ARs led to unusually high precipitation amounts at the coasts of Greenland and Svalbard. Over the sea ice northwest of Svalbard,

exceeding the climatology by a factor of 36. Not only is the intensity remarkable, but also the occurrence of rain over sea ice at this time of the yearthe rainfall indicated by ERA5 was a record-breaking event for mid-March.

The cold period was initialized after the passage of a strong cyclone over Svalbard on 21 March, when a northerly flow was established in the central region. Northerly winds pulled cold and dry air from the central Arctic into the North Atlantic, resulting in marine cold air outbreaks (MCAOs). We identified two strong MCAO periods (21–26 March and 01–02 April), where M partly exceeded the 90$^{\text{th}}$ percentile. The strong MCAOs were associated with high upward fluxes of sensible and latent heat in the unstable atmospheric boundary layer, which stress the interaction between the warm ocean and cold atmosphere. The ocean–atmosphere interactions in the boundary layer resulted in the typical high fraction of low-level cloud cover (cloud streets) and convective precipitation. After each strong MCAO period, aged warm air was advected to the measurement regions by a weaker northeasterly flow. During the aged warm air period, precipitation faded in the central region due to warming and drying. West of Svalbard, cloud-free conditions prevailed because of orographic lee effects (foehn). three MCAO events, separated by negative values of the MCAO index M. The second MCAO event, which started at the beginning of the cold period, lasted for 19 days, making it the tenth longest MCAO event in the climatology. The strength of the MCAO conditions in the central domain was related to the cyclone activity in the vicinity of this region.

After a weak MCAO, a Polar Low formed in the Fram Strait on 07 April. We confirmed that four out of six criteria for Polar Low development were fulfilled by inspecting the environmental conditions. With the help of dropsondes launched along a circle, we found strong rotation confined to the lowest 2 km despite negative relative vorticity in the eastern part related to lee effects. The Polar Low was located unusually far in the north. At the end of Despite the longer cold period, the entire campaign was on average warmer than the climatological mean. Thus, the cold period (10–12 April), warm and moist air was advected by a Scandinavian Low towards the southern region and diverted northwards through short-lived ARs and MWAIs dominated the anomaly signal, highlighting the importance of these events for the warming of the Arctic (Johansson et al., 2017). However, it must be noted that the ERA5 climatology may have systematic differences in 2022 compared to previous years as measurements from HALO-$(\mathcal{AC})^3$ dropsondes were assimilated. Furthermore, the quality and quantity of satellite measurements to be included in the assimilation improved over the years. Nevertheless, due to the low density of observations in the Arctic, using reanalyses is currently a well suited option for climatological comparisons.

Interestingly, precipitation was higher than the climatology for both periods as MCAOs also led to enhanced precipitation in the Fram Strait. The high altitude southerly winds transported cirrus clouds over the sea ice with cold and dry air from the Greenland ice sheet below. This combination resulted in an isolated humidity layer including Arctic cirrus in the absence of low- and mid-level clouds. Precipitation associated with MCAOs has been discussed as being responsible for differences between climate models and observations (von Lerber et al., 2022). However, precipitation is also difficult to measure accurately as MCAOs are mostly within the blind zone of satellite measurements (Schirmacher et al., 2023). Therefore, the quality of precipitation in reanalyses is of high interest. The detailed HALO-$(\mathcal{AC})^3$ remote sensing and in situ measurements can help to further constrain the representation of precipitation, including its phase, in the reanalysis.

With respect to the climatology, the entire campaign was slightly warmer considering both 2 m and 850 hPa temperatures, except for the central Fram Strait and north of Greenland. Here, 2 m temperature anomalies were negative. In the central

~~region, SICs were within the 10–90th percentiles of the climatology during the entire campaignperiod. The AR events caused remarkable reductions of SIC~~ Finally, we looked at the sea ice conditions and how they changed due to the different circulation patterns during the campaign. Overall, the marginal ice zone in the Fram Strait ~~and northeast of Svalbard due to dynamical forcing by wind and ocean, and possibly melt. Afterwards during the MCAO period, temperatures stayed below the freezing point and northerly winds increased SIC above the climatological meanin those regions . Only around Svalbard and at its southeastern coast, SICs were lower than the climatological mean values. We identified a strip of positive SIC anomaly in the central and western Fram Strait, which coincides well with negative 2 m temperature anomalies.~~

~~Atmospheric soundings and near–surface measurements at Ny–Ålesund generally represent the weather conditions of the central region well, when respecting the temporal delay of up to 1 day due to the propagation of synoptic systems during the warm period. However, during the cold period , lee effects at the coast of Svalbard cause cloud conditionsthat are only representative for the eastern part of the central region. The additional measurements at the AWIPEV can be implemented into the data analysis of HALO–(AC)^3 and provide a long–term climatological context to~~ had higher sea ice concentrations (SIC) compared to the ~~airborne measurements~~climatological mean, while the regions around Svalbard had lower SIC. MWAIs and ARs resulted in a reduction of SIC in the marginal ice zone below the climatological mean. The reduction was probably dominated by ice dynamics associated with the strong southerly winds, but melt was also possible because of temperatures above freezing. During the long period of MCAO conditions, the northerly winds and low temperatures led to a recovery of the SIC.

Compared to previous aircraft campaigns in the Arctic within ~~(AC)^3~~ ($\mathcal{AC}$)^3 that focused on the evolution of ~~(mixed–phase) clouds (ACLOUD; AFLUX and MOSAiC–ACA, Wendisch et al., 2019; Mech et al., 2022)~~mixed-phase) clouds (ACLOUD; AFLUX and , we observed a larger variety of MCAO conditions during ~~HALO–(AC)^3~~HALO-($\mathcal{AC}$)^3. The long phase of MCAOs with varying strength and different wind regimes provides opportunities for detailed MCAO studies making use of ~~the~~ airborne measurements. Also, the sea ice edge was closer to Svalbard than during AFLUX (March–April 2019) so that ocean–ice transects could be performed more easily. ~~We~~ HALO-($\mathcal{AC}$)^3 captured several MWAIs / ARs with unusual or even ~~record breaking~~ record-breaking strength. With regard to the changing climate when exchanges between the ~~mid–latitudes~~ mid–latitudes and the Arctic become more frequent~~and ARs are expected to shift poleward~~, the campaign provides a unique opportunity to study stronger than average MWAIs / ARs. ~~We conclude that~~ Thus, the weather conditions were well suited to achieve the objectives of the ~~HALO–(AC)^3~~ HALO-($\mathcal{AC}$)^3 campaign.

Code and data availability. All codes used for the analyses presented in this study have been uploaded to GITHUB and connected with ZENODO for public access (*in preparation*). Sea ice concentration climatology data is found on OSI SAF (2017) and Copernicus Climate Change Service (C3S) (2020). The high resolution sea ice concentration dataset used for 07 March–12 April 2022 is based on the product from the Institute of Environmental Physics, University of Bremen. The data is available at https://seaice.uni-bremen.de/data/modis_amsr2. ERA5 data on single and pressure levels can be accessed through Hersbach et al. (2018b) and Hersbach et al. (2018a). Ny-Ålesund radiosondes and ceilometer data have been published on PANGAEA (Maturilli and Kayser, 2016, 2017; Maturilli, 2020b, 2022). The Ny-Ålesund

precipitation data is provided by MET Norway and has been downloaded from https://seklima.met.no (last access 2023-11-30). Near-surface meteorology data from Ny-Ålesund is available on PANGAEA as well (Maturilli, 2020a). All data measured with HALO during HALO-$(\mathcal{AC})^3$ are currently being published on PANGAEA searchable via the tag "HALO-$(\mathcal{AC})^3$". A full description of the data set is in preparation.

Appendix A: ~~Methodology details~~

~~This part of the appendix includes additional details regarding the methods described in Sect. 2 that go beyond the necessary information to understand the study but help to reproduce the results.~~

~~For an exact computation of the regional averages over the southern, central and northern regions, we provide the geographical coordinates of the domains' boundaries in Table **??**.~~

~~Here, we describe the processing of variables to analyse the MCAO conditions (Sect. **??**) in greater detail for reproducibility. Turbulent flux data was confined to open water surfaces because our focus is on the intensity of the upward fluxes (positive sign) over open water during the MCAOs. We used the mean values over 1 hour at each grid point instead of the instantaneous values (Hersbach et al., 2020). For low, medium and high–level cloud cover, we computed the median value including 5, 25, 75, and 95$^{\text{th}}$ percentiles. Precipitation data was accumulated over 6 hour intervals and grouped into open water and sea ice covered surfaces. Snowfall is further separated into its large–scale and convective parts. The latter is defined in ERA5 as the frozen precipitation resulting from the convection scheme and thus from subgrid–scale convection. Total precipitation is then the sum of the convective and the large–scale part (Hersbach et al., 2020).~~

~~In the following, we summarize the meanings of the conditions tested for Polar Low formation (Sect. **??**) for better understanding: Condition C1 is a measure of the convection potential as it evaluates the mean temperature gradient between the surface and the mid–troposphere. Large differences between the 2 temperature and the SST (C2) promote strong sensible heat fluxes, stressing the air–sea interaction. Positive values of C3 represent an increase of potential temperature with height. At least conditionally unstable conditions (unstable (stable) for moisture–saturated (unsaturated) air parcels) should be present (C3 $\leq 3\,\mathrm{K\,km^{-1}}$). The relative humidity conditions C4$_{\mathrm{i}}$ and C4$_{\mathrm{ii}}$ are an important measure for the availability of moisture for latent heat release, a major energy source of a Polar Low. Maximum 10 m wind speed (C5) is an indicator of the Polar Low's strength. The geopotential height condition (C6) is selected to ensure the presence of an upper level trough.~~

~~Geographical coordinates for measurement regions as displayed in Fig. 1. Note that the northern part of the northern region in the central Arctic is extended to the west. Northern region Northern region extension Central region Southern region Northern limit in deg N 84.5 89.3 81.5 75.0 Southern limit in deg N 81.5 84.5 75.0 70.6 Western limit in deg E -9.0 -54.0 -9.0 0.0 Eastern limit in deg E 30.0 30.0 16.0 23.0~~

Appendix A: ~~Integrated water vapour transport for moist and warm air intrusions~~

Appendix A: Integrated water vapor transport for moist and warm air intrusions

~~For the MWAIs / ARs on 13 and 15~~ We show the total IVT from ERA5 for two snapshots of the ARs on 12–15 March, and for the ~~weaker~~ weak MWAI on 10 April ~~, we show the total IVT~~ in Fig. A1. While the ~~former two events~~ ARs on 12–15 March were meridionally aligned, the ~~latter~~ MWAI on 10 April had a rather zonal orientation. The strongest total IVT is found on 15 March, exceeding $400\,\mathrm{kg\,m^{-1}\,s^{-1}}$.

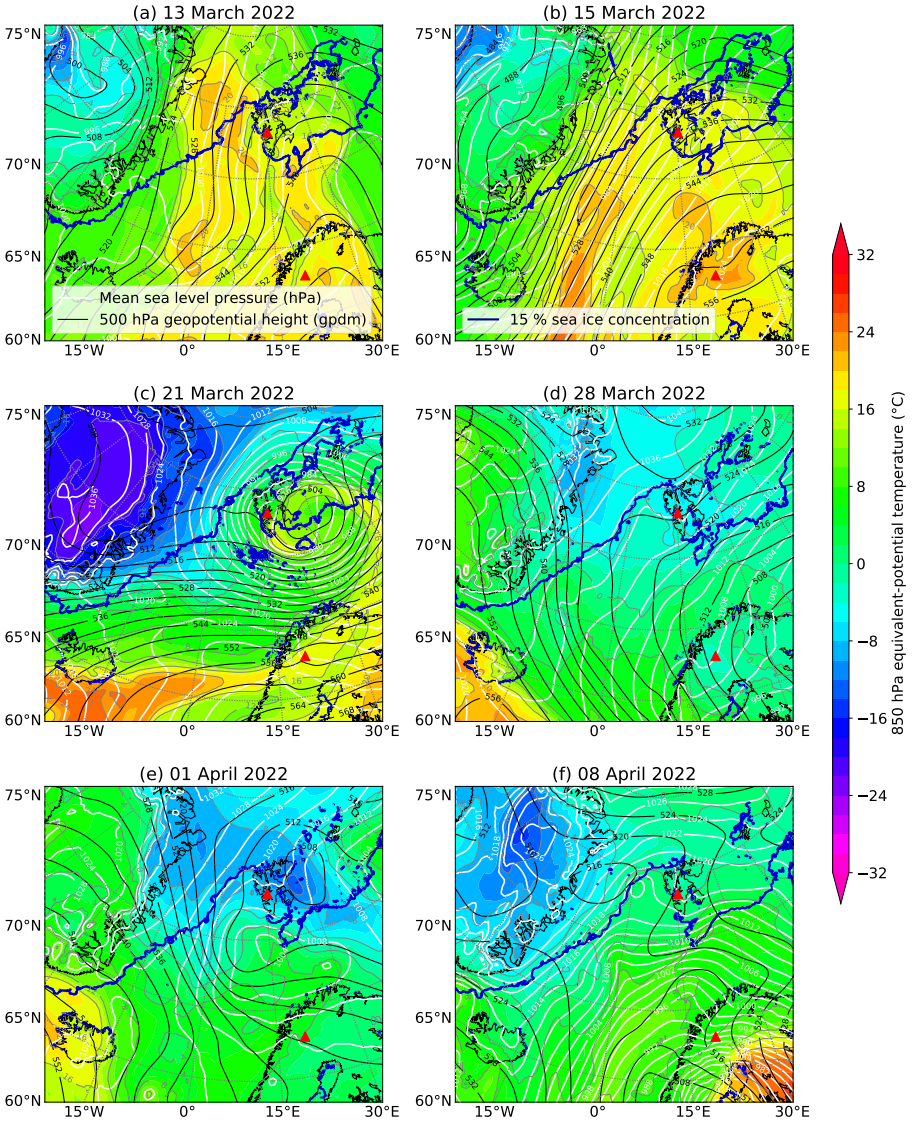

Figure 4. Maps of mean sea level pressure (white contour lines), 500 hPa geopotential height (black contour lines), and ~~*M*, the large scale pressure constellation, and regional averages of meteorological variables from ERA5 (Fig. ?? and ??). In Fig. ??, we show latitude–averages of IVT_{north} and the vertically integrated meridional heat flux IHT_{north} over the central region to spatially and temporally localize meridional heat and moisture transport corresponding with MWAIs and MCAOs. Negative values of IHT_{north} and IVT_{north} indicate southward fluxes. To put the weather conditions into climatological context, anomalies of temperature at~~ 850 ~~hPa~~ hPa equivalent-potential temperature (shading and ~~2 m above the surface, geopotential height at 500 hPa, and IWV were computed for the warm , cold and the entire campaign period. Positive (negative) anomalies correspond to values above (below) the long–term mean. Evaluating the temperature anomalies at these two levels reveals the vertical extent of the temperature anomalies in the lower troposphere~~ grey contours) from ERA5 data for representative days of the main weather conditions at 12 UTC. The 15 % sea ice concentration from AMSR2 (Spreen et al., 2008) is displayed as blue contour line.

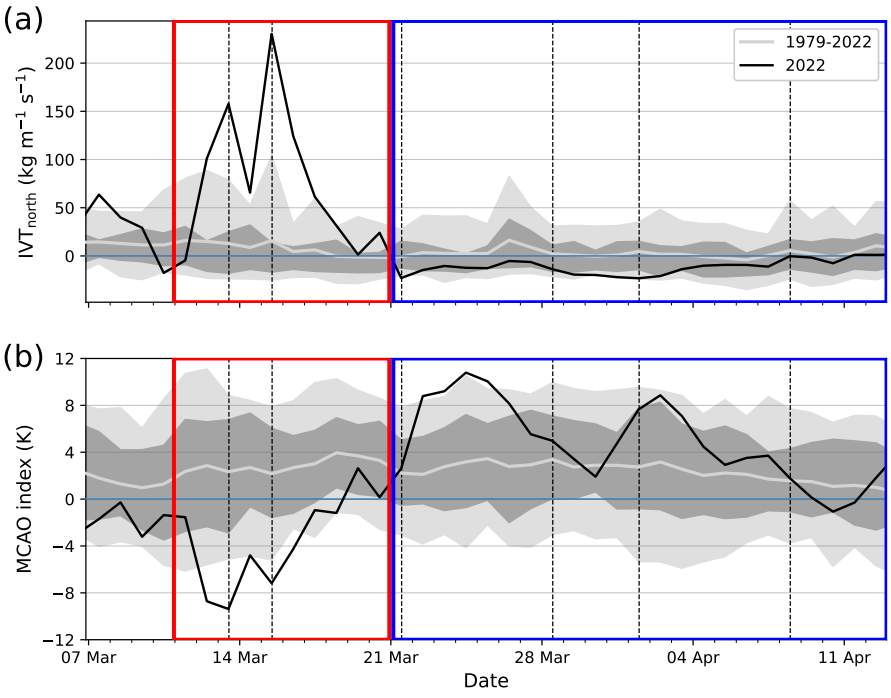

Figure 5. Daily ~~means~~ mean time series of (a) ~~northwards~~ northward component of integrated water ~~vapour~~ vapor transport (IVT_{north}), (b) Marine ~~Cold Air Outbreak~~ cold air outbreak (MCAO) index (M) based on ERA5 and averaged over the central region for ~~HALO~~ HALO-($\mathcal{AC}$)^3 (~~AC)^3 (~~black line). The mean, as well as the 10–90th and 25–75th percentiles of the climatology (1979–2022), are illustrated as grey ~~line~~lines, and light and dark grey shadings. The red (blue) box indicates the warm (cold) period dominated by ~~MWAIs~~ moist and warm air intrusions (~~MCAOs~~marine cold air outbreaks). Vertical dashed black lines mark the days shown in Fig. ~~??~~4.

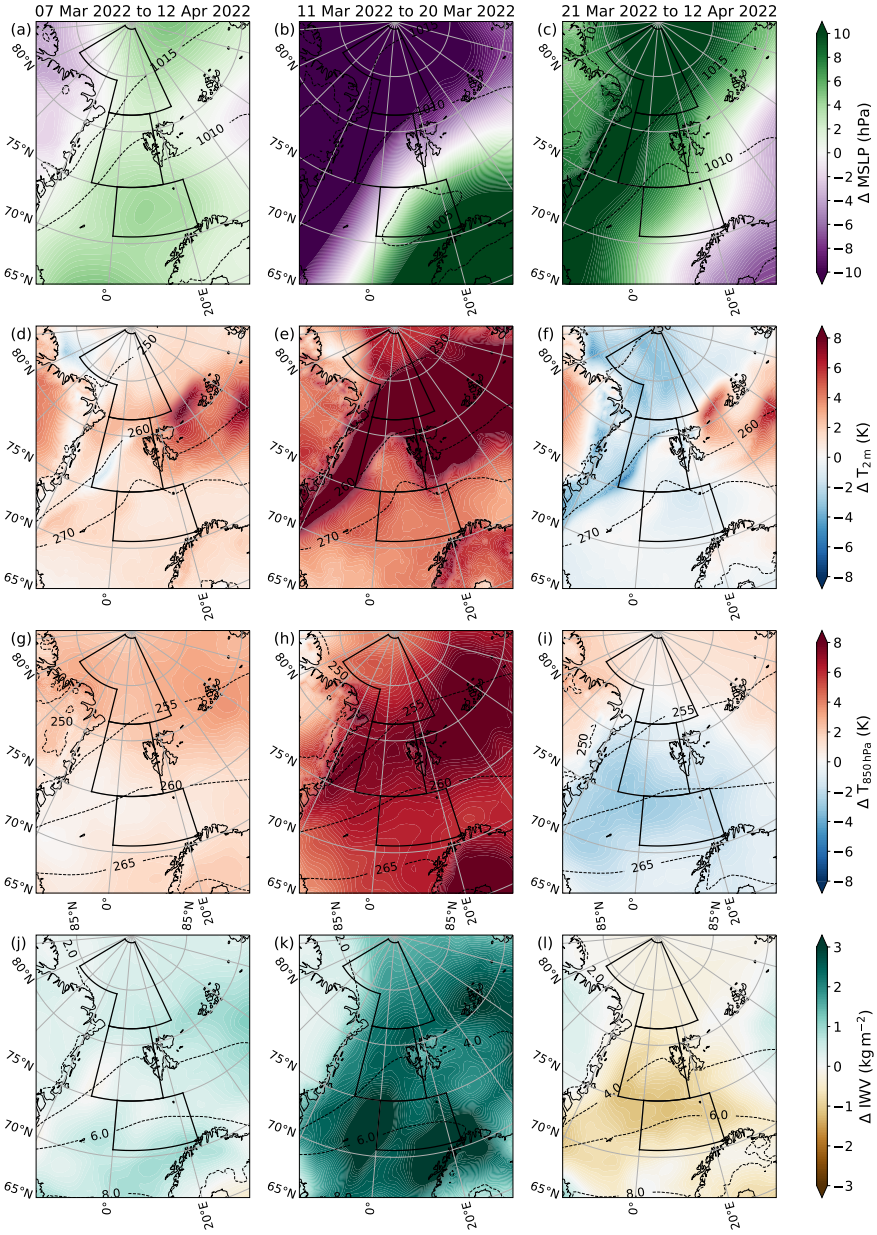

Figure 6. From top to bottom: Anomaly maps of mean sea level pressure (MSLP), 2 m temperature (ΔT_{2m}), 850 hPa temperature ($\Delta T_{850\,hPa}$), and integrated water vapor (ΔIWV) based on ERA5 for the entire campaign (left), the warm (middle), and the cold (right) period. The long-–term mean (1979–2022) is subtracted from the mean of the respective time period. Dashed black isolines describe the long—term climatology for the respective period in each panel. The three measurement regions (shown in Fig. 1) are illustrated as black boxes.

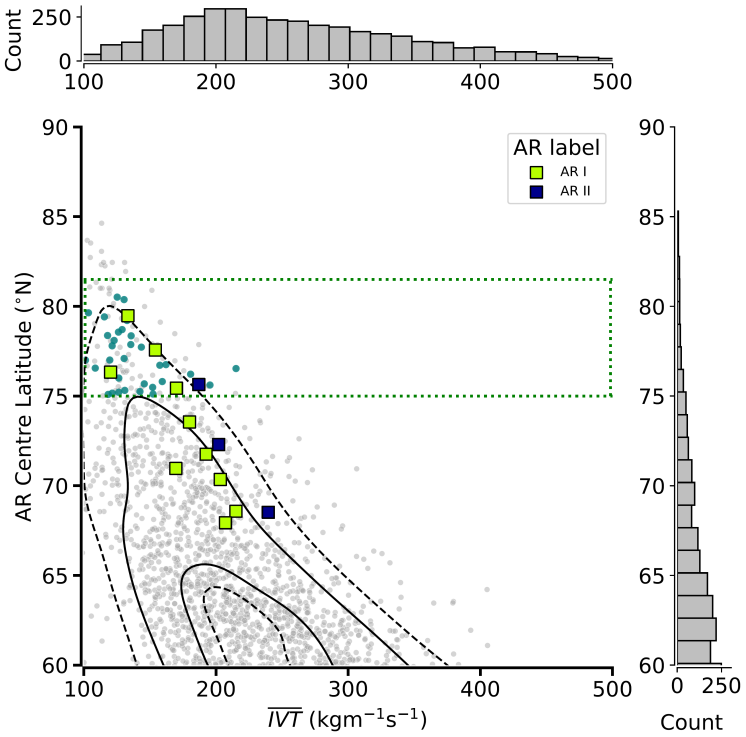

Figure 7. Six-hourly climatological (1979–2022) distribution of central latitudes of Atmospheric Rivers (ARs) as a function of mean AR integrated water vapor transport (IVT) using an ERA5-based AR catalog based on Guan and Waliser (2015). The analyzed area covers 60–90° N and 60° W–40° E. Blue dots mark ARs whose center was within the latitudes and longitudes of the central domain. Cases categorized as ARs during HALO-$(\mathcal{AC})^3$ are illustrated by colored squares. Black (dashed) lines indicate the 25th and 75th (10th and 90th) percentiles of a kernel density estimation to visualize the shape of the histogram. The green rectangle marks the latitudes of the central domain.

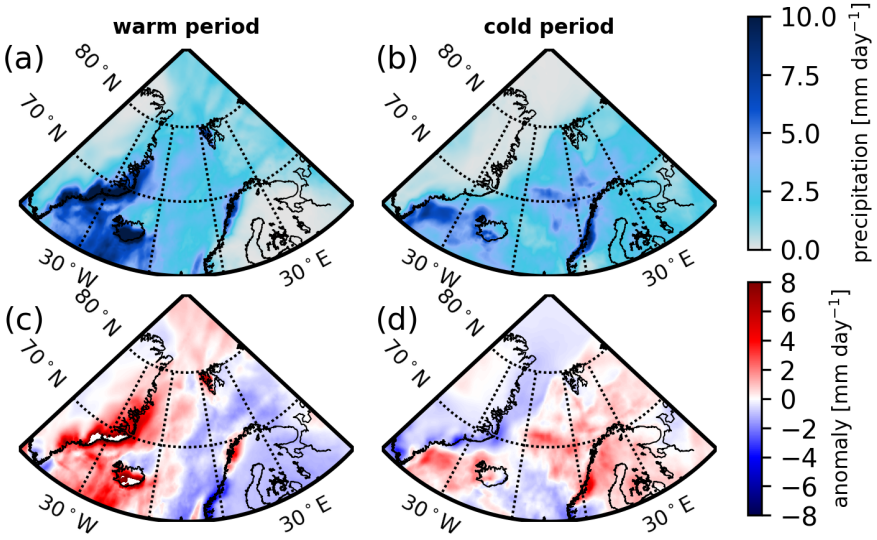

Figure 8. Hourly averaged total precipitation (sum of snowfall and rain rate) ($\mathrm{mm\,h^{-1}}$) (top row) and absolute deviations from the climatology (bottom row) derived from ERA5 for (a, c) the warm period, and (b, d) the cold period.

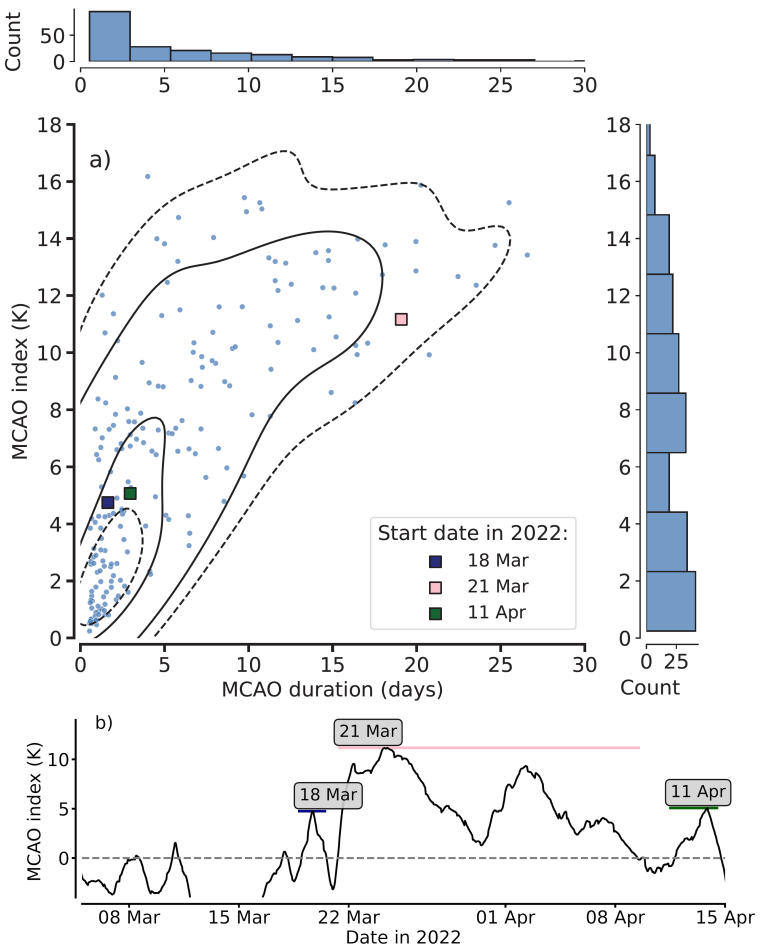

Figure 9. ~~Time series of Ny–Ålesund radiosondes of (~~a) ~~temperature profiles (shading), height of thermal tropopause (black line),~~ Two-dimensional histogram showing the ERA5-based duration and ~~wind barbs~~ strength of MCAOs in ~~selected levels,~~ the central domain for the period 1979–2022. Cases categorized during HALO-$(AC)^3$ are illustrated by colored squares and the legend entries of these cases indicate the start date. Black (~~b~~dashed) ~~specific humidity profiles (shading)~~ lines indicate the 25th and ~~resulting IWV~~ 75th (~~black line, right axis~~10th and 90th) ~~. Vertical dashed black lines indicate~~ percentiles of a kernel density estimation to visualize the ~~days shown in Fig~~shape of the histogram. ~~??. The red (blue~~b) ~~box indicates~~ MCAO index time series with higher temporal resolution and indicating the ~~shifted warm (cold~~MCAO periods marked in a)~~period~~.

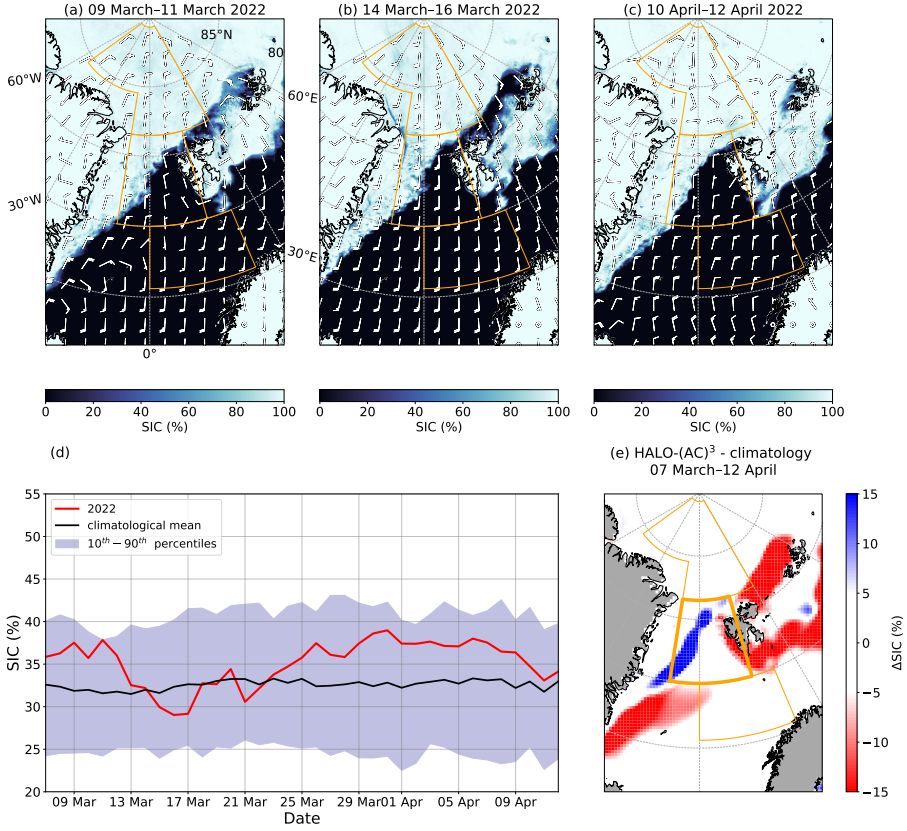

Figure 10. Average sea ice concentration (SIC) from the ~~MODIS-AMSR2~~ MODIS–AMSR2 product at 1 km grid resolution and 10 m wind speed (in knots) from ERA5 for (a) 09–11 March (prior to the first AR event), (b) 14–16 March (during the second AR event), (c) 10–12 April (at the end of the campaign). ~~Data is from the MODIS-AMSR2 product at 1 grid resolution~~Short (long) wind barbs represent wind speeds of 5 (10) knots. (d): SIC time series averaged over the central region for the campaign period, as well as the mean, and 10–90th percentiles of the 1979–2022 climatology. (e): SIC anomalies from the climatological mean averaged over the entire campaign period. Note that only differences larger 5 % are considered due to the uncertainties of the satellite product in the marginal ice zone. Data for (d) and (e) is from the OSI–SAF sea ice concentration climate data record.

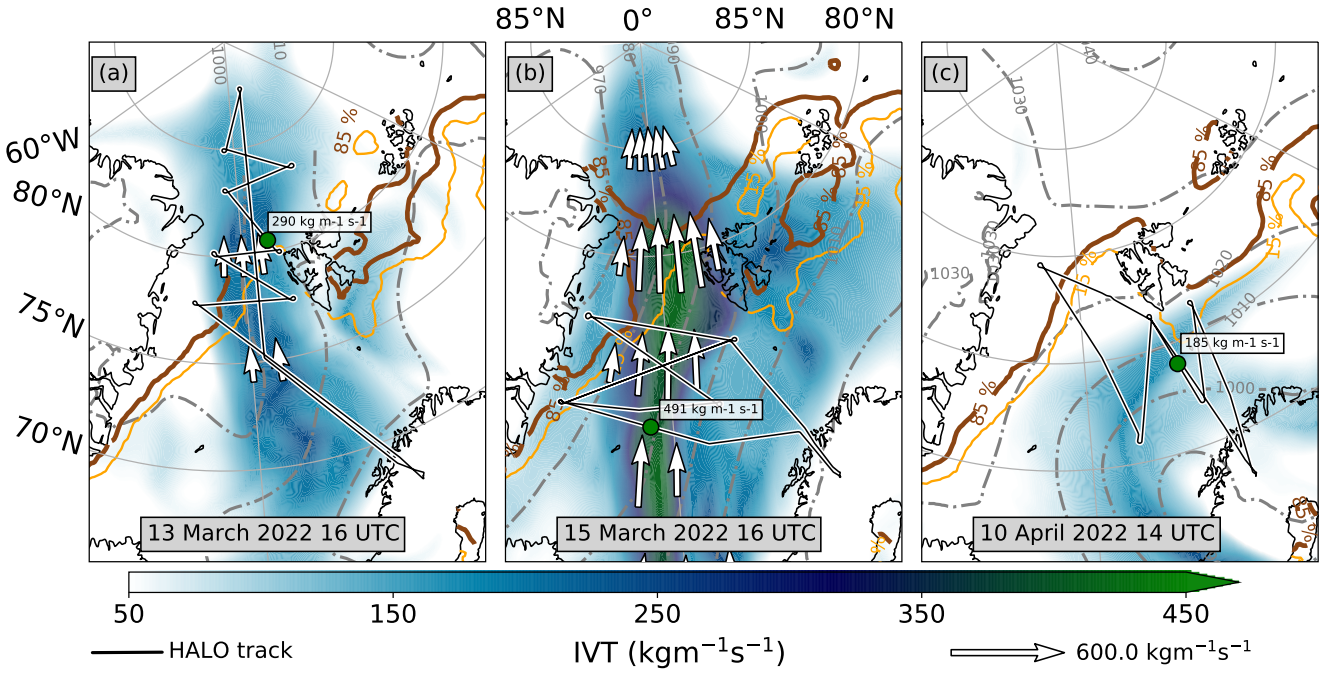

Figure A1. Total integrated water ~~vapour~~ vapor transport (IVT, zonal and meridional component) from ERA5 (colours) and dropsondes (circular marker) for ~~three~~ moist and warm air intrusions / Atmospheric Rivers: (a) 13 March 2022 16 UTC, (b) 15 March 2022 16 UTC, (c) 10 April 2022 14 UTC. Quivers ~~indicating~~ indicate the flow direction and strength, ~~as well as the HALO flight track (~~while black line with white outline ~~) are also included~~shows the HALO flight track. The orange (brown) line indicate the 15 % (85 %) sea ice concentration isoline. Grey ~~dash–dotted~~ dash-dotted contours show the mean sea level pressure. Data is based on ERA5.

Appendix B: ~~Moist and warm air intrusion trajectories~~

~~The general air flow on two selected MWAI / AR days is investigated. Three day back and two day forward trajectories shown in Fig. **??** are initialized on 13 and 15 March each at 18:00 UTC. The trajectories reveal that the air masses of the first MWAI day mainly originated from central Europe and the second case from the North Atlantic. Forward trajectories show that both MWAIs / ARs reached the central Arctic.~~

~~Three day backward and two day forward trajectories of the AR air masses observed in the central region on (a) 13 March 2022 18:00 UTC, and (b) 15 March 2022 18:00 UTC. at altitudes of 700, 850, and 925 hPa. Starting points are placed at 77.5° N between 20° W and 13° E with a zonal spacing of 1°. Both 72 hour back–trajectories as well as 48 hour forward–trajectories are computed. Grey shading indicates the sea ice concentration from ERA5.~~

Appendix B: ~~Marine cold air outbreak~~

~~Figure **??** shows the ERA5 based temporal evolution of temperature, relative humidity and wind for the eastern part of the northern region (identical western longitude boundary as the central region). The data has been processed as described in Sect. **??** and Appendix **??**. During the stronger MCAOs in the central region with northerly winds, the air masses originated from the northern region. Due to the low occurrence of northwesterly winds, the western extension of the northern region is not included. For comparison of turbulent fluxes between the central and southern region, we include Fig. **??**.~~

~~Temporal evolution of (a) wind, (b) air temperature (T), and (c) relative humidity (RH) on the 1000, 925, and 850 pressure levels as in Fig. **??**, but for the northern region (without western extension). Data is based on ERA5.~~

~~Temporal evolution of (a) wind, (b) air temperature (T), and (c) relative humidity (RH) on the 1000, 925, and 850 hPa pressure levels, and of (d) low–, (e) mid–, and (f) high–level cloud cover (CC), (g) precipitation, and (h) surface turbulent heat fluxes (STHF) as in Fig. **??** but for the southern region. Data is based on ERA5.~~

Appendix B: ~~Polar Low visual observations~~

~~Due to the relatively small extent of a Polar Low, we were able to see the entire structure during the HALO research flight on 08 April 2022. The photo was taken on one of the cross sections through the Polar Low, showing the relatively cloud free centre (eye) and the convective cloud band on its (north–)eastern side (Fig. **??**).~~

~~Photo of the Polar Low taken from HALO (portside) on 08 April 2022 at 09:57 UTC. The centre (eye) of the Polar Low can be seen in the foreground while the convective cloud band is visible in the background. The map indicates the flight track (black line) and the position of the aircraft at that time (red star). © Andreas Walbröl~~

Author contributions. SC, AE, IG, JanM, MW, and AW conceptualized the manuscript. MW and AW formulated the introduction with comments and input from AE, JanM, and SC. HD, BK, ML, NM, MM, JanR, and AW prepared the description of the data and methods

chapter. SB, HD, BK, ML, JanM, HM, RN, FP, JohR, JanR, IS, NS, and AW provided visualisations and analysed figures. JohM and AW collected codes from co-authors and made them publicly available. AW is the main author of this manuscript and ensured validation. All co-authors reviewed the manuscript.

Competing interests. The authors declare that they have no conflict of interest.

Acknowledgements. We gratefully acknowledge the funding by the Deutsche Forschungsgemeinschaft (DFG, German Research Foundation) for the ArctiC ~~Amplification~~amplification: Climate Relevant Atmospheric and SurfaCe Processes, and Feedback Mechanisms ~~(AC)^3~~ $(\mathcal{AC})^3$ Project Number 268020496 – TRR 172 within the Transregional Collaborative Research Center. We are further grateful for funding of project grant no. 316646266 by the Deutsche Forschungsgemeinschaft (DFG, German Research Foundation) within the framework of Priority Programme SPP 1294 to promote research with HALO. We thank the Institute of Environmental Physics, University of Bremen for the provision of the merged MODIS-AMSR2 sea–ice concentration data at https://seaice.uni-bremen.de/data/modis_amsr2 (last access 2023-04-04). Hersbach et al. (2018a) and Hersbach et al. (2018b) were downloaded from the Copernicus Climate Change Service (C3S) Climate Data Store. The results contain modified Copernicus Climate Change Service information 2022. Neither the European Commission nor ECMWF is responsible for any use that may be made of the Copernicus information or data it contains. We thank the Alfred Wegener Institute for providing and operating the two aircraft (Polar 5 and Polar 6), the crew, and also the technicians of the Polar 5 and Polar 6 aircraft. We are also grateful for the research aircraft HALO, the pilots and technicians provided and operated by the German Aerospace Centre (Deutsches Zentrum für ~~Luft–~~Luft- und Raumfahrt).

References

Avila-Diaz, A., Bromwich, D. H., Wilson, A. B., Justino, F., and Wang, S.-H.: Climate Extremes across the North American Arctic in Modern Reanalyses, J. Climate, 34, 2385–2410, https://doi.org/10.1175/JCLI-D-20-0093.1, 2021.

Bony, S. and Stevens, B.: Measuring Area-Averaged Vertical Motions with Dropsondes, J. Atmos. Sci., 76, 767–783, https://doi.org/10.1175/JAS-D-18-0141.1, 2019.

Bresson, H., Rinke, A., Mech, M., Reinert, D., Schemann, V., Ebell, K., Maturilli, M., Viceto, C., Gorodetskaya, I., and Crewell, S.: Case study of a moisture intrusion over the Arctic with the ICOsahedral Non-hydrostatic (ICON) model: resolution dependence of its representation, Atmos. Chem. Phys., 22, 173–196, https://doi.org/10.5194/acp-22-173-2022, 2022.

Cohen, J., Zhang, X., Francis, J., Jung, T., Kwok, R., Overland, J., Ballinger, T. J., Bhatt, U. S., Chen, H. W., Coumou, D., Feldstein, S., Gu, H., Handorf, D., Henderson, G., Ionita, M., Kretschmer, M., Laliberte, F., Lee, S., Linderholm, H. W., Maslowski, W., Peings, Y., Pfeiffer, K., Rigor, I., Semmler, T., Stroeve, J., Taylor, P. C., Vavrus, S., Vihma, T., Wang, S., Wendisch, M., Wu, Y., and Yoon, J.: Divergent consensuses on Arctic amplification influence on midlatitude severe winter weather, Nat. Clim. Change, 10, 20–29, https://doi.org/10.1038/s41558-019-0662-y, 2020.

Copernicus Climate Change Service (C3S): Sea ice concentration daily gridded data from 1979 to present derived from satellite observations, Copernicus Climate Change Service (C3S) Climate Data Store (CDS) [data set], https://doi.org/10.24381/CDS.3CD8B812, 2020.

Dahlke, S., Solbès, A., and Maturilli, M.: Cold Air Outbreaks in Fram Strait: Climatology, Trends, and Observations During an Extreme Season in 2020, J. Geophys. Res.: Atmos., 127, https://doi.org/10.1029/2021JD035741, 2022.

Di Biagio, C., Pelon, J., Blanchard, Y., Loyer, L., Hudson, S. R., Walden, V. P., Raut, J., Kato, S., Mariage, V., and Granskog, M. A.: Toward a Better Surface Radiation Budget Analysis Over Sea Ice in the High Arctic Ocean: A Comparative Study Between Satellite, Reanalysis, and local-scale Observations, J. Geophys. Res.: Atmos., 126, https://doi.org/10.1029/2020JD032555, 2021.

Drüe, C. and Heinemann, G.: High-resolution maps of the sea-ice concentration from MODIS satellite data, Geophys. Res. Lett., 31, L20 403, https://doi.org/10.1029/2004GL020808, 2004.

Fletcher, J., Mason, S., and Jakob, C.: The Climatology, Meteorology, and Boundary Layer Structure of Marine Cold Air Outbreaks in Both Hemispheres*, J. Climate, 29, 1999–2014, https://doi.org/10.1175/JCLI-D-15-0268.1, 2016.

Francis, J. A. and Vavrus, S. J.: Evidence for a wavier jet stream in response to rapid Arctic warming, Environ. Res. Lett., 10, 014 005, https://doi.org/10.1088/1748-9326/10/1/014005, 2015.

Geerts, B., Giangrande, S. E., McFarquhar, G. M., Xue, L., Abel, S. J., Comstock, J. M., Crewell, S., DeMott, P. J., Ebell, K., Field, P., et al.: The comble campaign: A study of marine boundary layer clouds in arctic cold-air outbreaks, Bulletin of the American Meteorological Society, 103, E1371–E1389, 2022.

George, G., Stevens, B., Bony, S., Pincus, R., Fairall, C., Schulz, H., Kölling, T., Kalen, Q. T., Klingebiel, M., Konow, H., Lundry, A., Prange, M., and Radtke, J.: JOANNE: Joint dropsonde Observations of the Atmosphere in tropical North atlaNtic meso-scale Environments, Earth Syst. Sci. Data, 13, 5253–5272, https://doi.org/10.5194/essd-13-5253-2021, 2021.

Gierens, R., Kneifel, S., Shupe, M. D., Ebell, K., Maturilli, M., and Löhnert, U.: Low-level mixed-phase clouds in a complex Arctic environment, Atmospheric Chemistry and Physics, 20, 3459–3481, https://doi.org/10.5194/acp-20-3459-2020, 2020.

Graham, R. M., Cohen, L., Ritzhaupt, N., Segger, B., Graversen, R. G., Rinke, A., Walden, V. P., Granskog, M. A., and Hudson, S. R.: Evaluation of Six Atmospheric Reanalyses over Arctic Sea Ice from Winter to Early Summer, J. Climate, 32, 4121–4143, https://doi.org/10.1175/JCLI-D-18-0643.1, 2019a.

Graham, R. M., Hudson, S. R., and Maturilli, M.: Improved Performance of ERA5 in Arctic Gateway Relative to Four Global Atmospheric Reanalyses, Geophys. Res. Lett., 46, 6138–6147, https://doi.org/10.1029/2019GL082781, 2019b.

Guan, B. and Waliser, D. E.: Detection of atmospheric rivers: Evaluation and application of an algorithm for global studies: Detection of Atmospheric Rivers, J. Geophys. Res.: Atmos., 120, 12 514–12 535, https://doi.org/10.1002/2015JD024257, 2015.

Guan, B. and Waliser, D. E.: Atmospheric rivers in 20 year weather and climate simulations: A multimodel, global evaluation, J. Geophys. Res.: Atmos., 122, 5556–5581, https://doi.org/10.1002/2016JD026174, 2017.

Guan, B., Waliser, D. E., and Ralph, F. M.: An Intercomparison between Reanalysis and Dropsonde Observations of the Total Water Vapor Transport in Individual Atmospheric Rivers, J. Hydrometeorol., 19, 321–337, https://doi.org/10.1175/JHM-D-17-0114.1, 2018.

Hartmann, J., Kottmeier, C., and Raasch, S.: Roll Vortices and Boundary-Layer Development during a Cold Air Outbreak, Boundary Layer Meteorol., 84, 45–65, https://doi.org/10.1023/A:1000392931768, 1997.

Hersbach, H., Bell, B., Berrisford, P., Biavati, G., Horányi, A., Muñoz Sabater, J., Nicolas, J., Peubey, C., Radu, R., Rozum, I., Schepers, D., Simmons, A., Soci, C., Dee, D., and Thépaut, J.-N.: ERA5 hourly data on pressure levels from 1959 to present, Copernicus Climate Change Service (C3S) Climate Data Store (CDS) [data set], https://doi.org/10.24381/cds.bd0915c6, 2018a.

Hersbach, H., Bell, B., Berrisford, P., Biavati, G., Horányi, A., Muñoz Sabater, J., Nicolas, J., Peubey, C., Radu, R., Rozum, I., Schepers, D., Simmons, A., Soci, C., Dee, D., and Thépaut, J.-N.: ERA5 hourly data on single levels from 1959 to present, Copernicus Climate Change Service (C3S) Climate Data Store (CDS) [data set], https://doi.org/10.24381/cds.adbb2d47, 2018b.

Hersbach, H., Bell, B., Berrisford, P., Hirahara, S., Horányi, A., Muñoz-Sabater, J., Nicolas, J., Peubey, C., Radu, R., Schepers, D., Simmons, A., Soci, C., Abdalla, S., Abellan, X., Balsamo, G., Bechtold, P., Biavati, G., Bidlot, J., Bonavita, M., Chiara, G., Dahlgren, P., Dee, D., Diamantakis, M., Dragani, R., Flemming, J., Forbes, R., Fuentes, M., Geer, A., Haimberger, L., Healy, S., Hogan, R. J., Hólm, E., Janisková, M., Keeley, S., Laloyaux, P., Lopez, P., Lupu, C., Radnoti, G., Rosnay, P., Rozum, I., Vamborg, F., Villaume, S., and Thépaut, J.: The ERA5 global reanalysis, Q. J. R. Meteorolog. Soc., 146, 1999–2049, https://doi.org/10.1002/qj.3803, 2020.

Hock, T. F. and Franklin, J. L.: The NCAR GPS Dropwindsonde, Bull. Am. Meteorol. Soc., 80, 407–420, https://doi.org/10.1175/1520-0477(1999)080<0407:TNGD>2.0.CO;2, 1999.

Hong, Y. and Liu, G.: The Characteristics of Ice Cloud Properties Derived from CloudSat and CALIPSO Measurements, J. Climate, 28, 3880–3901, https://doi.org/10.1175/JCLI-D-14-00666.1, 2015.

Johansson, E., Devasthale, A., Tjernström, M., Ekman, A. M. L., and L'Ecuyer, T.: Response of the lower troposphere to moisture intrusions into the Arctic, Geophys. Res. Lett., 44, 2527–2536, https://doi.org/10.1002/2017GL072687, 2017.

Kapsch, M.-L., Graversen, R. G., and Tjernström, M.: Springtime atmospheric energy transport and the control of Arctic summer sea-ice extent, Nat. Clim. Change, 3, 744–748, https://doi.org/10.1038/nclimate1884, 2013.

Kapsch, M.-L., Skific, N., Graversen, R. G., Tjernström, M., and Francis, J. A.: Summers with low Arctic sea ice linked to persistence of spring atmospheric circulation patterns, Clim. Dyn., 52, 2497–2512, https://doi.org/10.1007/s00382-018-4279-z, 2019.

Knudsen, E. M., Heinold, B., Dahlke, S., Bozem, H., Crewell, S., Gorodetskaya, I. V., Heygster, G., Kunkel, D., Maturilli, M., Mech, M., Viceto, C., Rinke, A., Schmithüsen, H., Ehrlich, A., Macke, A., Lüpkes, C., and Wendisch, M.: Meteorological conditions during the ACLOUD/PASCAL field campaign near Svalbard in early summer 2017, Atmospheric Chemistry and Physics, 18, 17 995–18 022, https://doi.org/10.5194/acp-18-17995-2018, 2018.

Kolstad, E. W., Bracegirdle, T. J., and Seierstad, I. A.: Marine cold-air outbreaks in the North Atlantic: temporal distribution and associations with large-scale atmospheric circulation, Clim. Dyn., 33, 187–197, https://doi.org/10.1007/s00382-008-0431-5, 2009.

Komatsu, K. K., Alexeev, V. A., Repina, I. A., and Tachibana, Y.: Poleward upgliding Siberian atmospheric rivers over sea ice heat up Arctic upper air, Sci. Rep., 8, 2872, https://doi.org/10.1038/s41598-018-21159-6, 2018.

Konow, H., Ewald, F., George, G., Jacob, M., Klingebiel, M., Kölling, T., Luebke, A. E., Mieslinger, T., Pörtge, V., Radtke, J., Schäfer, M., Schulz, H., Vogel, R., Wirth, M., Bony, S., Crewell, S., Ehrlich, A., Forster, L., Giez, A., Gödde, F., Groß, S., Gutleben, M., Hagen, M., Hirsch, L., Jansen, F., Lang, T., Mayer, B., Mech, M., Prange, M., Schnitt, S., Vial, J., Walbröl, A., Wendisch, M., Wolf, K., Zinner, T., Zöger, M., Ament, F., and Stevens, B.: EUREC^{4}A's HALO, Earth Syst. Sci. Data, 13, 5545–5563, https://doi.org/10.5194/essd-13-5545-2021, 2021.

Lauer, M., Mech, M., and Guan, B.: Global Atmospheric Rivers catalog for ERA5 reanalysis, https://doi.org/10.1594/PANGAEA.957161, 2023a.

Lauer, M., Rinke, A., Gorodetskaya, I., Sprenger, M., Mech, M., and Crewell, S.: Influence of atmospheric rivers and associated weather systems on precipitation in the Arctic, Atmos. Chem. Phys. [preprint], https://doi.org/10.5194/egusphere-2023-261, 2023-06-16, 2023b.

Lavergne, T., Sørensen, A. M., Kern, S., Tonboe, R., Notz, D., Aaboe, S., Bell, L., Dybkjær, G., Eastwood, S., Gabarro, C., Heygster, G., Killie, M. A., Brandt Kreiner, M., Lavelle, J., Saldo, R., Sandven, S., and Pedersen, L. T.: Version 2 of the EUMETSAT OSI SAF and ESA CCI sea-ice concentration climate data records, The Cryosphere, 13, 49–78, https://doi.org/10.5194/tc-13-49-2019, 2019.

Lee, S. H., Williams, P. D., and Frame, T. H. A.: Increased shear in the North Atlantic upper-level jet stream over the past four decades, Nature, 572, 639–642, https://doi.org/10.1038/s41586-019-1465-z, 2019.

Lenschow, D. H., Savic-Jovcic, V., and Stevens, B.: Divergence and Vorticity from Aircraft Air Motion Measurements, J. Atmos. Oceanic Technol., 24, 2062–2072, https://doi.org/10.1175/2007JTECHA940.1, 2007.

Lloyd, G., Choularton, T. W., Bower, K. N., Gallagher, M. W., Crosier, J., O'shea, S., Abel, S. J., Fox, S., Cotton, R., and Boutle, I. A.: In situ measurements of cloud microphysical and aerosol properties during the break-up of stratocumulus cloud layers in cold air outbreaks over the North Atlantic, Atmospheric Chemistry and Physics, 18, 17 191–17 206, 2018.

Ludwig, V., Spreen, G., and Pedersen, L. T.: Evaluation of a New Merged Sea-Ice Concentration Dataset at 1 km Resolution from Thermal Infrared and Passive Microwave Satellite Data in the Arctic, Remote Sens., 12, 3183, https://doi.org/10.3390/rs12193183, 2020.

Ma, W., Chen, G., and Guan, B.: Poleward Shift of Atmospheric Rivers in the Southern Hemisphere in Recent Decades, Geophys. Res. Lett., 47, https://doi.org/10.1029/2020GL089934, 2020.

Marsing, A., Meerkötter, R., Heller, R., Kaufmann, S., Jurkat-Witschas, T., Krämer, M., Rolf, C., and Voigt, C.: Investigating the radiative effect of Arctic cirrus measured in situ during the winter 2015–2016, Atmos. Chem. Phys., 23, 587–609, https://doi.org/10.5194/acp-23-587-2023, 2023.

Mattingly, K. S., Mote, T. L., and Fettweis, X.: Atmospheric River Impacts on Greenland Ice Sheet Surface Mass Balance, J. Geophys. Res.: Atmos., 123, 8538–8560, https://doi.org/10.1029/2018JD028714, 2018.

Mattingly, K. S., Mote, T. L., Fettweis, X., van As, D., Van Tricht, K., Lhermitte, S., Pettersen, C., and Fausto, R. S.: Strong Summer Atmospheric Rivers Trigger Greenland Ice Sheet Melt through Spatially Varying Surface Energy Balance and Cloud Regimes, J. Climate, 33, 6809–6832, https://doi.org/10.1175/JCLI-D-19-0835.1, 2020.

Maturilli, M.: Continuous meteorological observations at station Ny-Ålesund (2011-08 et seq), https://doi.org/10.1594/PANGAEA.914979, 2020a.

Maturilli, M.: High resolution radiosonde measurements from station Ny-Ålesund (2017-04 et seq), PANGAEA - Data Publisher for Earth & Environmental Science [data set], https://doi.org/10.1594/PANGAEA.914973, 2020b.

Maturilli, M.: Ceilometer cloud base height from station Ny-Ålesund (2017-08 et seq), PANGAEA - Data Publisher for Earth & Environmental Science [data set], https://doi.org/10.1594/PANGAEA.942331, 2022.

Maturilli, M. and Ebell, K.: Twenty-five years of cloud base height measurements by ceilometer in Ny-Ålesund, Svalbard, Earth Syst. Sci. Data, 10, 1451–1456, https://doi.org/10.5194/essd-10-1451-2018, 2018.

Maturilli, M. and Kayser, M.: Homogenized radiosonde record at station Ny-Ålesund, Spitsbergen, 1993-2014, PANGAEA - Data Publisher for Earth & Environmental Science [data set], https://doi.org/10.1594/PANGAEA.845373, 2016.

Maturilli, M. and Kayser, M.: Homogenized radiosonde record at station Ny-Ålesund, Spitsbergen, 2015-2016, PANGAEA - Data Publisher for Earth & Environmental Science [data set], https://doi.org/10.1594/PANGAEA.875196, 2017.

Maturilli, M., Herber, A., and König-Langlo, G.: Climatology and time series of surface meteorology in Ny-Ålesund, Svalbard, Earth Syst. Sci. Data, 5, 155–163, https://doi.org/10.5194/essd-5-155-2013, 2013.

Mech, M., Ehrlich, A., Herber, A., Lüpkes, C., Wendisch, M., Becker, S., Boose, Y., Chechin, D., Crewell, S., Dupuy, R., Gourbeyre, C., Hartmann, J., Jäkel, E., Jourdan, O., Kliesch, L.-L., Klingebiel, M., Kulla, B. S., Mioche, G., Moser, M., Risse, N., Ruiz-Donoso, E., Schäfer, M., Stapf, J., and Voigt, C.: MOSAiC-ACA and AFLUX - Arctic airborne campaigns characterizing the exit area of MOSAiC, Sci. Data, 9, 790, https://doi.org/10.1038/s41597-022-01900-7, 2022.

Mewes, D. and Jacobi, C.: Heat transport pathways into the Arctic and their connections to surface air temperatures, Atmos. Chem. Phys., 19, 3927–3937, https://doi.org/10.5194/acp-19-3927-2019, 2019.

Moreno-Ibáñez, M., Laprise, R., and Gachon, P.: Recent advances in polar low research: current knowledge, challenges and future perspectives, Tellus A: Dyn. Meteorol. Oceanogr., 73, 1890 412, https://doi.org/10.1080/16000870.2021.1890412, 2021.

Nash, D., Waliser, D., Guan, B., Ye, H., and Ralph, F. M.: The Role of Atmospheric Rivers in Extratropical and Polar Hydroclimate, J. Geophys. Res.: Atmos., 123, 6804–6821, https://doi.org/10.1029/2017JD028130, 2018.

Neff, W., Compo, G. P., Martin Ralph, F., and Shupe, M. D.: Continental heat anomalies and the extreme melting of the Greenland ice surface in 2012 and 1889: Melting of Greenland in 1889 and 2012, J. Geophys. Res.: Atmos., 119, 6520–6536, https://doi.org/10.1002/2014JD021470, 2014.

Newell, R. E., Newell, N. E., Zhu, Y., and Scott, C.: Tropospheric rivers? - A pilot study, Geophys. Res. Lett., 19, 2401–2404, https://doi.org/10.1029/92GL02916, 1992.

OSI SAF: Global Sea Ice Concentration Climate Data Record v2.0 - Multimission, EUMETSAT SAF on Ocean and Sea Ice [data set], https://doi.org/10.15770/EUM_SAF_OSI_0008, 2017.

Papritz, L. and Spengler, T.: A Lagrangian Climatology of Wintertime Cold Air Outbreaks in the Irminger and Nordic Seas and Their Role in Shaping Air–Sea Heat Fluxes, J. Climate, 30, 2717–2737, https://doi.org/10.1175/JCLI-D-16-0605.1, 2017.

Papritz, L., Aemisegger, F., and Wernli, H.: Sources and Transport Pathways of Precipitating Waters in Cold-Season Deep North Atlantic Cyclones, J. Atmos. Sci., 78, 3349–3368, https://doi.org/10.1175/JAS-D-21-0105.1, 2021.

Pithan, F., Medeiros, B., and Mauritsen, T.: Mixed-phase clouds cause climate model biases in Arctic wintertime temperature inversions, Clim. Dyn., 43, 289–303, https://doi.org/10.1007/s00382-013-1964-9, 2014.

Pithan, F., Svensson, G., Caballero, R., Chechin, D., Cronin, T. W., Ekman, A. M. L., Neggers, R., Shupe, M. D., Solomon, A., Tjernström, M., and Wendisch, M.: Role of air-mass transformations in exchange between the Arctic and mid-latitudes, Nat. Geosci., 11, 805–812, https://doi.org/10.1038/s41561-018-0234-1, 2018.

Radovan, A., Crewell, S., Moster Knudsen, E., and Rinke, A.: Environmental conditions for polar low formation and development over the Nordic Seas: study of January cases based on the Arctic System Reanalysis, Tellus A: Dyn. Meteorol. Oceanogr., 71, 1618 131, https://doi.org/10.1080/16000870.2019.1618131, 2019.

Rantanen, M., Karpechko, A. Y., Lipponen, A., Nordling, K., Hyvärinen, O., Ruosteenoja, K., Vihma, T., and Laaksonen, A.: The Arctic has warmed nearly four times faster than the globe since 1979, Commun. Earth Environ., 3, 168, https://doi.org/10.1038/s43247-022-00498-3, 2022.

Rasmussen, E. A. and Turner, J.: Polar lows: Mesoscale weather systems in the polar regions, Cambridge University Press, 2003.

Rückert, J. E., Rostosky, P., Huntemann, M., Clemens-Sewall, D., Ebell, K., Kaleschke, L., Lemmetyinen, J., Macfarlane, A. R., Naderpour, R., Stroeve, J., Walbröl, A., and Spreen, G.: Sea ice concentration satellite retrievals influenced by surface changes due to warm air intrusions: A case study from the MOSAiC expedition, Elem. Sci. Anth., EarthArXiv [preprint], https://doi.org/10.31223/X5VW85, 2023-03-24, 2023.

Schirmacher, I., Kollias, P., Lamer, K., Mech, M., Pfitzenmaier, L., Wendisch, M., and Crewell, S.: Assessing Arctic low-level clouds and precipitation from above – a radar perspective, Atmospheric Measurement Techniques, 16, 4081–4100, https://doi.org/10.5194/amt-16-4081-2023, 2023.

Screen, J. A. and Simmonds, I.: The central role of diminishing sea ice in recent Arctic temperature amplification, Nature, 464, 1334–1337, https://doi.org/10.1038/nature09051, 2010.

Serreze, M. C. and Barry, R. G.: Processes and impacts of Arctic amplification: A research synthesis, Global Planet. Change, 77, 85–96, https://doi.org/10.1016/j.gloplacha.2011.03.004, 2011.

Serreze, M. C., Barrett, A. P., Stroeve, J. C., Kindig, D. N., and Holland, M. M.: The emergence of surface-based Arctic amplification, The Cryosphere, 3, 11–19, https://doi.org/10.5194/tc-3-11-2009, 2009.

Serreze, M. C., Gustafson, J., Barrett, A. P., Druckenmiller, M. L., Fox, S., Voveris, J., Stroeve, J., Sheffield, B., Forbes, B. C., Rasmus, S., et al.: Arctic rain on snow events: bridging observations to understand environmental and livelihood impacts, Environmental Research Letters, 16, 105 009, 2021.

Shapiro, M. A. and Keyser, D.: Fronts, Jet Streams and the Tropopause, in: Extratropical Cyclones, edited by Newton, C. W. and Holopainen, E. O., pp. 167–191, American Meteorological Society, Boston, MA, https://doi.org/10.1007/978-1-944970-33-8_10, 1990.

Shestakova, A. A., Chechin, D. G., Lüpkes, C., Hartmann, J., and Maturilli, M.: The foehn effect during easterly flow over Svalbard, Atmos. Chem. Phys., 22, 1529–1548, https://doi.org/10.5194/acp-22-1529-2022, 2022.

Spreen, G. and Kern, S.: Methods of satellite remote sensing of sea ice, in: Sea Ice, edited by Thomas, D. N., pp. 239–260, John Wiley & Sons, Ltd, Chichester, UK, https://doi.org/10.1002/9781118778371.ch9, 2016.

Spreen, G., Kaleschke, L., and Heygster, G.: Sea ice remote sensing using AMSR-E 89-GHz channels, J. Geophys. Res.: Oceans, 113, C02S03, https://doi.org/10.1029/2005JC003384, 2008.

Sprenger, M. and Wernli, H.: The LAGRANTO Lagrangian analysis tool – version 2.0, Geosci. Model Dev., 8, 2569–2586, https://doi.org/10.5194/gmd-8-2569-2015, 2015.

Stendel, M., Francis, J., White, R., Williams, P. D., and Woollings, T.: The jet stream and climate change, in: Climate Change, pp. 327–357, Elsevier, https://doi.org/10.1016/B978-0-12-821575-3.00015-3, 2021.

Stevens, B., Ament, F., Bony, S., Crewell, S., Ewald, F., Gross, S., Hansen, A., Hirsch, L., Jacob, M., Kölling, T., Konow, H., Mayer, B., Wendisch, M., Wirth, M., Wolf, K., Bakan, S., Bauer-Pfundstein, M., Brueck, M., Delanoë, J., Ehrlich, A., Farrell, D., Forde, M., Gödde, F., Grob, H., Hagen, M., Jäkel, E., Jansen, F., Klepp, C., Klingebiel, M., Mech, M., Peters, G., Rapp, M., Wing, A. A., and Zinner, T.:

A High-Altitude Long-Range Aircraft Configured as a Cloud Observatory: The NARVAL Expeditions, Bull. Am. Meteorol. Soc., 100, 1061–1077, https://doi.org/10.1175/BAMS-D-18-0198.1, 2019.

Stevens, B., Bony, S., Farrell, D., Ament, F., Blyth, A., Fairall, C., Karstensen, J., Quinn, P. K., Speich, S., Acquistapace, C., Aemisegger, F., Albright, A. L., Bellenger, H., Bodenschatz, E., Caesar, K.-A., Chewitt-Lucas, R., De Boer, G., Delanoë, J., Denby, L., Ewald, F., Fildier, B., Forde, M., George, G., Gross, S., Hagen, M., Hausold, A., Heywood, K. J., Hirsch, L., Jacob, M., Jansen, F., Kinne, S., Klocke, D., Kölling, T., Konow, H., Lothon, M., Mohr, W., Naumann, A. K., Nuijens, L., Olivier, L., Pincus, R., Pöhlker, M., Reverdin, G., Roberts, G., Schnitt, S., Schulz, H., Siebesma, A. P., Stephan, C. C., Sullivan, P., Touzé-Peiffer, L., Vial, J., Vogel, R., Zuidema, P., Alexander, N., Alves, L., Arixi, S., Asmath, H., Bagheri, G., Baier, K., Bailey, A., Baranowski, D., Baron, A., Barrau, S., Barrett, P. A., Batier, F., Behrendt, A., Bendinger, A., Beucher, F., Bigorre, S., Blades, E., Blossey, P., Bock, O., Böing, S., Bosser, P., Bourras, D., Bouruet-Aubertot, P., Bower, K., Branellec, P., Branger, H., Brennek, M., Brewer, A., Brilouet, P.-E., Brügmann, B., Buehler, S. A., Burke, E., Burton, R., Calmer, R., Canonici, J.-C., Carton, X., Cato Jr., G., Charles, J. A., Chazette, P., Chen, Y., Chilinski, M. T., Choularton, T., Chuang, P., Clarke, S., Coe, H., Cornet, C., Coutris, P., Couvreux, F., Crewell, S., Cronin, T., Cui, Z., Cuypers, Y., Daley, A., Damerell, G. M., Dauhut, T., Deneke, H., Desbios, J.-P., Dörner, S., Donner, S., Douet, V., Drushka, K., Dütsch, M., Ehrlich, A., Emanuel, K., Emmanouilidis, A., Etienne, J.-C., Etienne-Leblanc, S., Faure, G., Feingold, G., Ferrero, L., Fix, A., Flamant, C., Flatau, P. J., Foltz, G. R., Forster, L., Furtuna, I., Gadian, A., Galewsky, J., Gallagher, M., Gallimore, P., Gaston, C., Gentemann, C., Geyskens, N., Giez, A., Gollop, J., Gouirand, I., Gourbeyre, C., De Graaf, D., De Groot, G. E., Grosz, R., Güttler, J., Gutleben, M., Hall, K., Harris, G., Helfer, K. C., Henze, D., Herbert, C., Holanda, B., Ibanez-Landeta, A., Intrieri, J., Iyer, S., Julien, F., Kalesse, H., Kazil, J., Kellman, A., Kidane, A. T., Kirchner, U., Klingebiel, M., Körner, M., Kremper, L. A., Kretzschmar, J., Krüger, O., Kumala, W., Kurz, A., L'Hégaret, P., Labaste, M., Lachlan-Cope, T., Laing, A., Landschützer, P., Lang, T., Lange, D., Lange, I., Laplace, C., Lavik, G., Laxenaire, R., Le Bihan, C., Leandro, M., Lefevre, N., Lena, M., Lenschow, D., Li, Q., Lloyd, G., Los, S., Losi, N., Lovell, O., Luneau, C., Makuch, P., Malinowski, S., Manta, G., Marinou, E., Marsden, N., Masson, S., Maury, N., Mayer, B., Mayers-Als, M., Mazel, C., McGeary, W., McWilliams, J. C., Mech, M., Mehlmann, M., Meroni, A. N., Mieslinger, T., Minikin, A., Minnett, P., Möller, G., Morfa Avalos, Y., Muller, C., Musat, I., Napoli, A., Neuberger, A., Noisel, C., Noone, D., Nordsiek, F., Nowak, J. L., Oswald, L., Parker, D. J., Peck, C., Person, R., Philippi, M., Plueddemann, A., Pöhlker, C., Pörtge, V., Pöschl, U., Pologne, L., Posyniak, M., Prange, M., Quiñones Meléndez, E., Radtke, J., Ramage, K., Reimann, J., Renault, L., Reus, K., Reyes, A., Ribbe, J., Ringel, M., Ritschel, M., Rocha, C. B., Rochetin, N., Röttenbacher, J., Rollo, C., Royer, H., Sadoulet, P., Saffin, L., Sandiford, S., Sandu, I., Schäfer, M., Schemann, V., Schirmacher, I., Schlenczek, O., Schmidt, J., Schröder, M., Schwarzenboeck, A., Sealy, A., Senff, C. J., Serikov, I., Shohan, S., Siddle, E., Smirnov, A., Späth, F., Spooner, B., Stolla, M. K., Szkółka, W., De Szoeke, S. P., Tarot, S., Tetoni, E., Thompson, E., Thomson, J., Tomassini, L., Totems, J., Ubele, A. A., Villiger, L., Von Arx, J., Wagner, T., Walther, A., Webber, B., Wendisch, M., Whitehall, S., Wiltshire, A., Wing, A. A., Wirth, M., Wiskandt, J., Wolf, K., Worbes, L., Wright, E., Wulfmeyer, V., Young, S., Zhang, C., Zhang, D., Ziemen, F., Zinner, T., and Zöger, M.: EUREC4A, Earth System Science Data, 13, 4067–4119, https://doi.org/10.5194/essd-13-4067-2021, 2021.

Stoll, P. J.: A global climatology of polar lows investigated for local differences and wind-shear environments, Weather Clim. Dyn., 3, 483–504, https://doi.org/10.5194/wcd-3-483-2022, 2022.

Stroeve, J., Nandan, V., Willatt, R., Dadic, R., Rostosky, P., Gallagher, M., Mallett, R., Barrett, A., Hendricks, S., Tonboe, R., McCrystall, M., Serreze, M., Thielke, L., Spreen, G., Newman, T., Yackel, J., Ricker, R., Tsamados, M., Macfarlane, A., Hannula, H.-R., and Schneebeli, M.: Rain on snow (ROS) understudied in sea ice remote sensing: a multi-sensor analysis of ROS during MOSAiC (Multidisciplinary drifting Observatory for the Study of Arctic Climate), The Cryosphere, 16, 4223–4250, https://doi.org/10.5194/tc-16-4223-2022, 2022.

Terpstra, A., Michel, C., and Spengler, T.: Forward and Reverse Shear Environments during Polar Low Genesis over the Northeast Atlantic, Mon. Weather Rev., 144, 1341–1354, https://doi.org/10.1175/MWR-D-15-0314.1, 2016.

Terpstra, A., Renfrew, I. A., and Sergeev, D. E.: Characteristics of Cold Air Outbreak events and associated Polar Mesoscale Cyclogenesis over the North Atlantic region, J. Climate, pp. 1–52, https://doi.org/10.1175/JCLI-D-20-0595.1, 2021.

Tjernström, M., Shupe, M. D., Brooks, I. M., Persson, P. O. G., Prytherch, J., Salisbury, D. J., Sedlar, J., Achtert, P., Brooks, B. J., Johnston, P. E., Sotiropoulou, G., and Wolfe, D.: Warm-air advection, air mass transformation and fog causes rapid ice melt: WARM-AIR ADVECTION, FOG AND ICE MELT, Geophys. Res. Lett., 42, 5594–5602, https://doi.org/10.1002/2015GL064373, 2015.

Viceto, C., Gorodetskaya, I. V., Rinke, A., Maturilli, M., Rocha, A., and Crewell, S.: Atmospheric rivers and associated precipitation patterns during the ACLOUD and PASCAL campaigns near Svalbard (May–June 2017): case studies using observations, reanalyses, and a regional climate model, Atmos. Chem. Phys., 22, 441–463, https://doi.org/10.5194/acp-22-441-2022, 2022.

von Lerber, A., Mech, M., Rinke, A., Zhang, D., Lauer, M., Radovan, A., Gorodetskaya, I., and Crewell, S.: Evaluating seasonal and regional distribution of snowfall in regional climate model simulations in the Arctic, Atmospheric Chemistry and Physics, 22, 7287–7317, https://doi.org/10.5194/acp-22-7287-2022, 2022.

Wahl, S., Bollmeyer, C., Crewell, S., Figura, C., Friederichs, P., Hense, A., Keller, J. D., and Ohlwein, C.: A novel convective-scale regional reanalysis COSMO-REA2: Improving the representation of precipitation, metz, 26, 345–361, https://doi.org/10.1127/metz/2017/0824, 2017.

Wang, C., Graham, R. M., Wang, K., Gerland, S., and Granskog, M. A.: Comparison of ERA5 and ERA-Interim near-surface air temperature, snowfall and precipitation over Arctic sea ice: effects on sea ice thermodynamics and evolution, The Cryosphere, 13, 1661–1679, https://doi.org/10.5194/tc-13-1661-2019, 2019.

Wendisch, M., Macke, A., Ehrlich, A., Lüpkes, C., Mech, M., Chechin, D., Dethloff, K., Velasco, C. B., Bozem, H., Brückner, M., Clemen, H.-C., Crewell, S., Donth, T., Dupuy, R., Ebell, K., Egerer, U., Engelmann, R., Engler, C., Eppers, O., Gehrmann, M., Gong, X., Gottschalk, M., Gourbeyre, C., Griesche, H., Hartmann, J., Hartmann, M., Heinold, B., Herber, A., Herrmann, H., Heygster, G., Hoor, P., Jafariserajehlou, S., Jäkel, E., Järvinen, E., Jourdan, O., Kästner, U., Kecorius, S., Knudsen, E. M., Köllner, F., Kretzschmar, J., Lelli, L., Leroy, D., Maturilli, M., Mei, L., Mertes, S., Mioche, G., Neuber, R., Nicolaus, M., Nomokonova, T., Notholt, J., Palm, M., van Pinxteren, M., Quaas, J., Richter, P., Ruiz-Donoso, E., Schäfer, M., Schmieder, K., Schnaiter, M., Schneider, J., Schwarzenböck, A., Seifert, P., Shupe, M. D., Siebert, H., Spreen, G., Stapf, J., Stratmann, F., Vogl, T., Welti, A., Wex, H., Wiedensohler, A., Zanatta, M., and Zeppenfeld, S.: The Arctic Cloud Puzzle: Using ACLOUD/PASCAL Multiplatform Observations to Unravel the Role of Clouds and Aerosol Particles in Arctic Amplification, Bull. Am. Meteorol. Soc., 100, 841–871, https://doi.org/10.1175/BAMS-D-18-0072.1, 2019.

Wendisch, M., Handorf, D., Tegen, I., Neggers, R., and Spreen, G.: Glimpsing the Ins and Outs of the Arctic Atmospheric Cauldron, Eos, 102, https://doi.org/10.1029/2021EO155959, 2021.

Wendisch, M., Brückner, M., Crewell, S., Ehrlich, A., Notholt, J., Lüpkes, C., Macke, A., Burrows, J. P., Rinke, A., Quaas, J., Maturilli, M., Schemann, V., Shupe, M. D., Akansu, E. F., Barrientos-Velasco, C., Bärfuss, K., Blechschmidt, A.-M., Block, K., Bougoudis, I., Bozem, H., Böckmann, C., Bracher, A., Bresson, H., Bretschneider, L., Buschmann, M., Chechin, D. G., Chylik, J., Dahlke, S., Deneke, H., Dethloff, K., Donth, T., Dorn, W., Dupuy, R., Ebell, K., Egerer, U., Engelmann, R., Eppers, O., Gerdes, R., Gierens, R., Gorodetskaya, I. V., Gottschalk, M., Griesche, H., Gryanik, V. M., Handorf, D., Harm-Altstädter, B., Hartmann, J., Hartmann, M., Heinold, B., Herber, A., Herrmann, H., Heygster, G., Höschel, I., Hofmann, Z., Hölemann, J., Hünerbein, A., Jafariserajehlou, S., Jäkel, E., Jacobi, C., Janout, M., Jansen, F., Jourdan, O., Jurányi, Z., Kalesse-Los, H., Kanzow, T., Käthner, R., Kliesch, L. L., Klingebiel, M., Knudsen, E. M., Kovács, T., Körtke, W., Krampe, D., Kretzschmar, J., Kreyling, D., Kulla, B., Kunkel, D., Lampert, A., Lauer, M., Lelli, L., von Lerber, A., Linke,

O., Löhnert, U., Lonardi, M., Losa, S. N., Losch, M., Maahn, M., Mech, M., Mei, L., Mertes, S., Metzner, E., Mewes, D., Michaelis, J., Mioche, G., Moser, M., Nakoudi, K., Neggers, R., Neuber, R., Nomokonova, T., Oelker, J., Papakonstantinou-Presvelou, I., Pätzold, F., Pefanis, V., Pohl, C., van Pinxteren, M., Radovan, A., Rhein, M., Rex, M., Richter, A., Risse, N., Ritter, C., Rostosky, P., Rozanov, V. V., Donoso, E. R., Saavedra Garfias, P., Salzmann, M., Schacht, J., Schäfer, M., Schneider, J., Schnierstein, N., Seifert, P., Seo, S., Siebert, H., Soppa, M. A., Spreen, G., Stachlewska, I. S., Stapf, J., Stratmann, F., Tegen, I., Viceto, C., Voigt, C., Vountas, M., Walbröl, A., Walter, M., Wehner, B., Wex, H., Willmes, S., Zanatta, M., and Zeppenfeld, S.: Atmospheric and Surface Processes, and Feedback Mechanisms Determining Arctic Amplification: A Review of First Results and Prospects of the (AC)3 Project, Bull. Am. Meteorol. Soc., 104, E208–E242, https://doi.org/10.1175/BAMS-D-21-0218.1, 2023.

Wendisch, M., Crewell, S., Ehrlich, A., Herber, A., Kirbus, B., Lüpkes, C., Mech, M., Abel, S. J., Akansu, E. F., Ament, F., Aubry, C., Becker, S., Borrmann, S., Bozem, H., Brückner, M., Clemen, H.-C., Dahlke, S., Dekoutsidis, G., Delanoë, J., De La Torre Castro, E., Dorff, H., Dupuy, R., Eppers, O., Ewald, F., George, G., Gorodetskaya, I. V., Grawe, S., Groß, S., Hartmann, J., Henning, S., Hirsch, L., Jäkel, E., Joppe, P., Jourdan, O., Jurányi, Z., Karalis, M., Kellermann, M., Klingebiel, M., Lonardi, M., Lucke, J., Luebke, A., Maahn, M., Maherndl, N., Maturilli, M., Mayer, B., Mayer, J., Mertes, S., Michaelis, J., Michalkov, M., Mioche, G., Moser, M., Müller, H., Neggers, R., Ori, D., Paul, D., Paulus, F., Pilz, C., Pithan, F., Pöhlker, M., Pörtge, V., Ringel, M., Risse, N., Roberts, G. C., Rosenburg, S., Röttenbacher, J., Rückert, J., Schäfer, M., Schäfer, J., Schemannn, V., Schirmacher, I., Schmidt, J., Schmidt, S., Schneider, J., Schnitt, S., Schwarz, A., Siebert, H., Sodemann, H., Sperzel, T., Spreen, G., Stevens, B., Stratmann, F., Svensson, G., Tatzelt, C., Tuch, T., Vihma, T., Voigt, C., Volkmer, L., Walbröl, A., Weber, A., Wehner, B., Wetzel, B., Wirth, M., and Zinner, T.: Overview: Quasi-Lagrangian observations of Arctic air mass transformations – Introduction and initial results of the HALO–$(AC)^3$ aircraft campaign, EGUsphere, 2024, 1–46, https://doi.org/10.5194/egusphere-2024-783, 2024.

Wesche, C., Steinhage, D., and Nixdorf, U.: Polar aircraft Polar5 and Polar6 operated by the Alfred Wegener Institute, JLSRF, 2, A87, https://doi.org/10.17815/jlsrf-2-153, 2016.

Woods, C. and Caballero, R.: The Role of Moist Intrusions in Winter Arctic Warming and Sea Ice Decline, J. Climate, 29, 4473–4485, https://doi.org/10.1175/JCLI-D-15-0773.1, 2016.

Woods, C., Caballero, R., and Svensson, G.: Large-scale circulation associated with moisture intrusions into the Arctic during winter: Moisture Intrusions during Arctic Winter, Geophys. Res. Lett., 40, 4717–4721, https://doi.org/10.1002/grl.50912, 2013.

You, C., Tjernström, M., Devasthale, A., and Steinfeld, D.: The Role of Atmospheric Blocking in Regulating Arctic Warming, Geophys. Res. Lett., 49, https://doi.org/10.1029/2022GL097899, 2022.

Yu, Y., Xiao, W., Zhang, Z., Cheng, X., Hui, F., and Zhao, J.: Evaluation of 2-m Air Temperature and Surface Temperature from ERA5 and ERA-I Using Buoy Observations in the Arctic during 2010–2020, Remote Sens., 13, 2813, https://doi.org/10.3390/rs13142813, 2021.

Zahn, M. and von Storch, H.: A long-term climatology of North Atlantic polar lows, Geophys. Res. Lett., 35, L22 702, https://doi.org/10.1029/2008GL035769, 2008.

Ziereis, H. and Gläßer, M.: HALO - Global Player für die Atmosphärenforschung, Deutsches Zentrum für Luft- und Raumfahrt (DLR), https://elib.dlr.de/51508/, 2006.